BASS. XXII. The BASS DR2 AGN catalog and data

Koss, M.J.; Ricci, C.; Trakhtenbrot, B.; Oh, K.; den Brok, J.S.; Mejía-Restrepo, J.E.; ... ; Williams, J.

The Astrophysical Journal Supplement Series, 261:2 (30pp), 2022 July https://doi.org/10.3847/1538-4365/ac6c05

BASS. XXII. The BASS DR2 AGN Catalog and Data

Michael J. Koss[1,2], Claudio Ricci[3,4], Benny Trakhtenbrot[5], Kyuseok Oh[6,7,37], Jakob S. den Brok[8,9], Julian E. Mejía-Restrepo[10], Daniel Stern[11], George C. Privon[12,13], Ezequiel Treister[14], Meredith C. Powell[15], Richard Mushotzky[16], Franz E. Bauer[2,17,18], Tonima T. Ananna[19], Mislav Baloković[20], Rudolf E. Bär[8], George Becker[21], Patricia Bessiere[14], Leonard Burtscher[22], Turgay Caglar[22], Enrico Congiu[23], Phil Evans[24], Fiona Harrison[25], Marianne Heida[26], Kohei Ichikawa[27,28,29], Nikita Kamraj[25], Isabella Lamperti[30], Fabio Pacucci[31,32], Federica Ricci[14,33], Rogério Riffel[34], Alejandra F. Rojas[35], Kevin Schawinski[36], Matthew J. Temple[3], C. Megan Urry[20], Sylvain Veilleux[16], and Jonathan Williams[16]

[1] Eureka Scientific, 2452 Delmer Street, Suite 100, Oakland, CA 94602-3017, USA; mike.koss@eurekasci.com
[2] Space Science Institute, 4750 Walnut Street, Suite 205, Boulder, CO 80301, USA
[3] Núcleo de Astronomía de la Facultad de Ingeniería, Universidad Diego Portales, Av. Ejército Libertador 441, Santiago 22, Chile
[4] Kavli Institute for Astronomy and Astrophysics, Peking University, Beijing 100871, People's Republic of China
[5] School of Physics and Astronomy, Tel Aviv University, Tel Aviv 69978, Israel
[6] Korea Astronomy & Space Science institute, 776, Daedeokdae-ro, Yuseong-gu, Daejeon 34055, Republic of Korea
[7] Department of Astronomy, Kyoto University, Kitashirakawa-Oiwake-cho, Sakyo-ku, Kyoto 606-8502, Japan
[8] Institute for Particle Physics and Astrophysics, ETH Zürich, Wolfgang-Pauli-Strasse 27, CH-8093 Zürich, Switzerland
[9] Argelander Institute for Astronomy, Auf dem Hügel 71, D-53231, Bonn, Germany
[10] European Southern Observatory, Casilla 19001, Santiago 19, Chile
[11] Jet Propulsion Laboratory, California Institute of Technology, 4800 Oak Grove Drive, MS 169-224, Pasadena, CA 91109, USA
[12] National Radio Astronomy Observatory, 520 Edgemont Road, Charlottesville, VA 22903, USA
[13] Department of Astronomy, University of Florida, P.O. Box 112055, Gainesville, FL 32611, USA
[14] Instituto de Astrofísica, Facultad de Física, Pontificia Universidad Católica de Chile, Casilla 306, Santiago 22, Chile
[15] Kavli Institute of Particle Astrophysics and Cosmology, Stanford University, 452 Lomita Mall, Stanford, CA 94305, USA
[16] Department of Astronomy and Joint Space-Science Institute, University of Maryland, College Park, MD 20742, USA
[17] Instituto de Astrofísica and Centro de Astroingeniería, Facultad de Física, Pontificia Universidad Católica de Chile, Casilla 306, Santiago 22, Chile
[18] Millennium Institute of Astrophysics (MAS), Nuncio Monseñor Sótero Sanz 100, Providencia, Santiago, Chile
[19] Department of Physics and Astronomy, Dartmouth College, 6127 Wilder Laboratory, Hanover, NH 03755, USA
[20] Yale Center for Astronomy & Astrophysics and Department of Physics, Yale University, P.O. Box 208120, New Haven, CT 06520-8120, USA
[21] Department of Physics & Astronomy, University of California, Riverside, CA 92521, USA
[22] Leiden Observatory, P.O. Box 9513, 2300 RA, Leiden, The Netherlands
[23] Departamento de Astronomía, Universidad de Chile, Camino del Observatorio 1515, Las Condes, Santiago, Chile
[24] Department of Physics and Astronomy, University of Leicester, Leicester, LE1 7RH, UK
[25] Cahill Center for Astronomy and Astrophysics, California Institute of Technology, Pasadena, CA 91125, USA
[26] European Southern Observatory, Karl-Schwarzschild-Str. 2, D-85748 Garching bei München, Germany
[27] Frontier Research Institute for Interdisciplinary Sciences, Tohoku University, Sendai 980-8578, Japan
[28] Astronomical Institute, Graduate School of Science Tohoku University, 6-3 Aramaki, Aoba-ku, Sendai 980-8578, Japan
[29] Max-Planck-Institut für extraterrestrische Physik (MPE), Giessenbachstrasse 1, D-85748 Garching bei Müunchen, Germany
[30] Centro de Astrobiología (CAB), CSIC-INTA, Cra. de Ajalvir Km. 4, E-28850 Torrejón de Ardoz, Madrid, Spain
[31] Center for Astrophysics, Harvard & Smithsonian, Cambridge, MA 02138, USA
[32] Black Hole Initiative, Harvard University, Cambridge, MA 02138, USA
[33] Dipartimento di Fisica e Astronomia, Università di Bologna, via Gobetti 93/2, I-40129 Bologna, Italy
[34] Departamento de Astronomia, Instituto de Física, Universidade Federal do Rio Grande do Sul, CP 15051, 91501-970, Porto Alegre, RS, Brazil
[35] Centro de Astronomía (CITEVA), Universidad de Antofagasta, Avenida Angamos 601, Antofagasta, Chile
[36] Modulos AG, Technoparkstrasse 1, CH-8005 Zurich, Switzerland
Received 2021 September 3; revised 2022 April 2; accepted 2022 April 10; published 2022 July 15

Abstract

We present the active galactic nucleus (AGN) catalog and optical spectroscopy for the second data release of the Swift BAT AGN Spectroscopic Survey (BASS DR2). With this DR2 release we provide 1449 optical spectra, of which 1182 are released for the first time, for the 858 hard-X-ray-selected AGNs in the Swift BAT 70-month sample. The majority of the spectra (801/1449, 55%) are newly obtained from Very Large Telescope (VLT)/X-shooter or Palomar/Doublespec. Many of the spectra have both higher resolution ($R > 2500$, $N \sim 450$) and/or very wide wavelength coverage (3200–10000 Å, $N \sim 600$) that are important for a variety of AGN and host galaxy studies. We include newly revised AGN counterparts for the full sample and review important issues for population studies, with 47 AGN redshifts determined for the first time and 790 black hole mass and accretion rate estimates. This release is spectroscopically complete for all AGNs (100%, 858/858), with 99.8% having redshift measurements (857/858) and 96% completion in black hole mass estimates of unbeamed AGNs (722/752). This AGN sample represents a unique census of the brightest hard-X-ray-selected AGNs in the sky, spanning many

[37] JSPS Fellow.

orders of magnitude in Eddington ratio ($L/L_{\rm Edd} = 10^{-5}$–100), black hole mass ($M_{\rm BH} = 10^5$–$10^{10}\,M_\odot$), and AGN bolometric luminosity ($L_{\rm bol} = 10^{40}$–10^{47} erg s^{-1}).

Unified Astronomy Thesaurus concepts: X-ray active galactic nuclei (2035); Active galactic nuclei (16); Seyfert galaxies (1447); X-ray quasars (1821); X-ray surveys (1824); Surveys (1671); Sky surveys (1464); Galaxy spectroscopy (2171)

Supporting material: machine-readable tables

1. Introduction

Many different optical spectroscopic surveys have been done of active galactic nuclei (AGNs) in X-ray survey fields. Early work focused on bright sources from the Einstein (e.g., Stocke et al. 1991) and ROSAT surveys (e.g., Voges et al. 1999) typically focused on obtaining basic redshift and counterpart information for tens to hundreds of sources. This was later extended to deeper and fainter sources in Chandra fields (e.g., Green et al. 2004; Szokoly et al. 2004; Eckart et al. 2006; Treister et al. 2009; Silverman et al. 2010) or XMM-Newton surveys (e.g., Menzel et al. 2016). Full spectroscopic completeness was difficult in the deepest surveys owing to the optical faintness of distant targets (Brandt & Hasinger 2005). More recently, these efforts have focused on direct estimates of supermassive black hole (BH) masses for X-ray-selected AGNs with broad emission lines using virial relations (e.g., Shen et al. 2011).

Larger optical spectroscopic samples of X-ray-selected AGNs now exist within the Sloan Digital Sky Survey (SDSS) footprint, though typically focused on unobscured AGNs. A total of 7005 ROSAT sources were crossmatched with the SDSS spectroscopic footprint (Anderson et al. 2007). Due to the soft X-ray sensitivity of ROSAT (e.g., 0.1–2.4 keV), the majority, 89% (6224/7005), were broad-line AGNs. Similarly, a study by Mahony et al. (2010) in the southern hemisphere using spectra from the Six Degree Field Galaxy Survey (Jones et al. 2004, 2009), a near-infrared-selected redshift survey covering a large area in the southern hemisphere (∼17,000 deg^2), had spectroscopic identifications for 1715 ROSAT sources in the southern hemisphere. More recently, SPectroscopic IDentification of eROSITA Sources (SPIDERS; Dwelly et al. 2017; Comparat et al. 2020) is currently collecting 40,000 spectra of X-ray-selected AGNs from ROSAT and the XMM slew survey (0.5–12 keV), which is more sensitive to obscured AGNs.

Hard X-ray emission (>10 keV) from the corona of the AGN can probe the innermost parts of the central engine of AGNs with the advantage over UV/optical/soft X-rays that it can even find AGNs in highly obscured (e.g., $N_{\rm H} > 10^{22}$–10^{25} cm^{-2}) systems. The Swift BAT survey (Barthelmy et al. 2005), with its all-sky coverage that is insensitive to obscuration up to Compton-thick levels (Koss et al. 2016a), provides the largest, most complete sample of bright, local ($z < 0.1$), powerful AGNs. The spectroscopic coverage in the SDSS for BAT AGNs is, however, only ∼15% (Koss et al. 2017). Therefore, a complete optical spectroscopic sample of BAT AGNs, including the unobscured to the highly obscured AGNs that are largely absent from ROSAT surveys, provides a unique way to fully understand BH growth and its relation to the host galaxy. The BAT AGN survey also provides a bright complement that is more sensitive to obscured AGNs compared to the currently ongoing eROSITA satellite mission and its all-sky survey (Predehl et al. 2021).

The goal of the BAT AGN Spectroscopic Survey (BASS) is to provide the largest available spectroscopic sample of Swift BAT ultrahard X-ray (14–195 keV) detected AGNs. In the BASS DR1 (Koss et al. 2017), mostly archival optical telescope data were used for 641 BAT AGNs from the 70-month BAT catalog (Baumgartner et al. 2013) and 102 AGNs composing the near-IR (NIR) DR1 (Lamperti et al. 2017). These data were then used in a variety of scientific studies, such as between X-ray emission and high-ionization optical lines (Berney et al. 2015), ionized gas outflows (Rojas et al. 2020), and radio emission (Baek et al. 2019; Smith et al. 2020). Several works identified the importance of the Eddington ratio in various scaling relations (e.g., Oh et al. 2017; Ricci et al. 2017b, 2018) and links to host galaxy properties such as molecular gas (Koss et al. 2021).

In the BASS data release 2 (DR2), we have identified all AGNs among the 1210 sources in the BAT 70-month survey in order to obtain a 100% spectroscopically complete sample of high-quality optical spectra and BH mass estimates for a large fraction of AGNs across the entire sky. High signal-to-noise ratio (S/N) and spectral resolution optical spectroscopy with measurements of continuum, emission, and absorption lines, over the full optical range (3200–10000 Å), provides a large number of important diagnostics. To name a few, these include star formation rates, stellar masses, stellar population ages, dust reddening, metallicities, AGN-driven outflows, and dynamical properties of the galaxy such as velocity dispersions of stellar populations (e.g., Tremonti et al. 2004; Vazdekis et al. 2012; Yates et al. 2012; Shimizu et al. 2018; Rojas et al. 2020). Repeat optical spectroscopy can also probe the time-variable nature of these emission components such as in changing optical type AGNs (e.g., Collin-Souffrin et al. 1973; Shappee et al. 2014).

In this first catalog paper of the DR2 release series, we provide an updated list of counterparts and the 1449 optical spectra of 858 AGNs among the 1210 sources in the BAT 70-month survey (Baumgartner et al. 2013). We provide an explanation of all the optical spectra obtained, their reductions, and general derived measurements. An overview of the DR2 release and scientific results and a comparison with other surveys are provided in Koss et al. (2022a). Further catalogs of derived measurements will be provided in subsequent papers, such as broad-line measurements (Mejía-Restrepo et al. 2022), narrow emission line measurements from the best available optical spectra (Oh et al. 2022), velocity dispersion measurements from stellar absorption lines (Koss et al. 2022b), and the NIR spectroscopic measurements (Ricci et al. 2022; den Brok et al. 2022). We will also provide scientific investigations using DR2 data such as the BH mass and Eddington ratio distribution function for obscured and unobscured AGNs (Ananna et al. 2022), the ability of the MIR to recover obscured AGNs (Pfeifle et al. 2022), and the $M_{\rm BH}$–$\sigma_\star$ relation of type 1 unobscured AGNs (T. Caglar et al. 2022, in preparation). Throughout this work, we adopt $\Omega_{\rm M} = 0.3$, $\Omega_\Lambda = 0.7$, and $H_0 = 70$ km s^{-1} Mpc^{-1}. To determine extinction

due to Milky Way foreground dust, we use the maps of Schlegel et al. (1998) and the extinction law derived by Cardelli et al. (1989) with $R_v = 3.1$.

2. Revised AGN Catalog

The initial 70-month catalog (Baumgartner et al. 2013) was composed of 1210 sources, including 822 classified as AGNs or associated with a galaxy and likely an AGN, 287 Galactic sources (e.g., high/low-mass X-ray binary, cataclysmic variable, pulsar), 19 clusters, and 82 unknown sources. The counterpart positions and AGN classifications were updated based on WISE and X-ray data for 838 AGNs in the BASS DR1 (see Appendix A, Ricci et al. 2017a), which included three dual AGN systems. However, even after the DR1, 44 unknown BAT sources, typically near the Galactic plane ($|b| < 10°$), had not been associated with counterparts. Here we discuss the BASS DR2 AGN counterparts after an extensive examination of the remaining unknown 70-month catalog sources and important issues for surveys of these AGNs.

Given the large (FWHM = 19.′5) Swift BAT point-spread function (PSF), it is important to consider cases such as chance alignment of multiple AGNs, AGN clustering, and dual AGNs for population studies. Due to the scarcity of Swift BAT sources in the sky, the likelihood of chance alignment of any two unassociated sources within the BAT beam is small. Specifically, there are ∼850 sources at $|b| > 5°$ (91% of the sky), so the likelihood of chance alignment of one unassociated source within the BAT beam is very small, ∼0.2%. However, there are some unique cases involving galaxy mergers (e.g., Koss et al. 2018) and galaxy clustering where multiple AGN systems occur. Additionally, at lower fluxes, where AGNs are more numerous, there may be some cases of flux boosting where two sources below the sky sensitivity both contribute to be above the detection sensitivity.

Throughout this work, we refer to AGNs as Sy1 (with optical broad Hβ), Sy1.9 (narrow Hβ and broad Hα), and Sy2 (with narrow Hβ and narrow Hα, including small numbers of LINERs and AGNs in H_2-dominated regions). This nomenclature is used for the sake of simplicity and consistency with previous work, despite the fact that many of our BASS DR2 AGNs may not be considered as Seyfert galaxies, given their high (X-ray) luminosities. Additionally, a small number of Sy2 sources would be better classified as HII or LINERs or composites based on their position in the BPT diagram (Koss et al. 2017), or even elusive AGNs (Smith et al. 2014), due to a lack of prominent lines. These classifications are discussed in detail in the BASS DR2 paper on narrow emission line measurements (Oh et al. 2022). Finally, some Sy2 sources with narrow optical lines are known to have polarized broad lines or NIR broad lines (e.g., Lamperti et al. 2017).

2.1. Newly Identified AGNs and Galactic Sources

There were still some unidentified sources listed in the 70-month catalog, typically within the Galactic plane, that were not part of the BASS DR1 sample. We examined them all to ensure that our sample provided a complete census of all AGNs detected with Swift BAT across the sky. Further optical spectroscopy found many of them to be stellar in nature.

We uncovered an additional 22 AGNs among the remaining unidentified sources (Table 1). These sources were the brightest 2–10 keV sources within the 5′ Swift BAT position error circle, and optical spectroscopy confirmed their AGN nature. The total sample then increases from 838 to 858 AGNs.[38] Further details on the X-ray modeling of these newly detected AGNs will be provided in C. Ricci et al. (2022, in preparation).

A summary of the 17 sources that are newly classified as Galactic is provided in Table 2. For 10/17 sources, we determine the stellar nature based on optical spectroscopy, with the remaining sources being classified in recent publications.

There are two cases that were thought to be AGNs based on only an X-ray and WISE detection in the BASS DR1, but optical follow-up (Figure 1) found the source to be Galactic. SWIFT J0428.2−6704A was found to be an eclipsing X-ray binary (Kennedy et al. 2020), which follow-up optical spectra confirmed. We observed SWIFT J1535.8−5749 (aka IGR J15360−5750) but found the source to be consistent with a very red star based on the Ca II triplet spectral region (8450–8700 Å) and CO band heads (2.29–2.51 μm).

In the other 15 cases, the 70-month X-ray classification was uncertain (Baumgartner et al. 2013), but the sources were found to be Galactic. For instance, SWIFT J0630.9+1129 showed a very red star with Hα emission at $z = 0$. SWIFT J1213.2−6020 (aka IGR J12134−6015) was found to be located within 0.″3 of 2MASS J12132397−6015169 based on Chandra (Karasev et al. 2012). The WISE and X-ray counterpart has a Gaia source within 1″ with 1.4 ± 0.055 mas parallax and spectra consistent with a star.

2.2. Excluded Unknown Sources in the Galactic Plane

The DR2 sample defined here is fully complete for all BAT 70-month BAT AGNs and unknown sources above ($|b| > 3°$) or below $A_V = 5$ mag. Beyond these limits an additional seven sources were excluded (Table 3) in the analysis owing to their very high extinction values (5–43 A_V mag).

Many of these sources have been surveyed extensively as part of INTEGRAL surveys (e.g., Tomsick et al. 2008). These sources are very close to the Galactic plane, with many foreground stars and very high extinction levels that make any accurate optical targeting impractical, though they may host AGNs in some cases. A follow-up Chandra observation of SWIFT J1848.5−0046 (aka IGR J18485−0047) showed a source coincident with strong radio emission consistent with an AGN (Tomsick et al. 2009). SWIFT J1403.6−6146 (aka IGR J14044−6146) was observed with Chandra, but no detection was found after an earlier Swift XRT detection, suggesting variability that may be associated with an AGN (Bodaghee et al. 2012). In one case (SWIFT J2037.2+4151), optical spectral follow-up showed a very red spectrum, but there was no obvious counterpart. SWIFT J2056.8+4939 (aka 4C 49.35) has both radio emission and a likely Fermi detection consistent with a blazar-like beamed AGN. None of the remaining sources have been observed with Chandra, XMM-Newton, or NuSTAR. Further source localization and characterization with Chandra, deeper X-ray observations with XMM-Newton or NuSTAR, radio, and finally NIR spectroscopy will likely be required to identify these sources and their possible AGN nature.

There was also one remaining 70-month transient source outside the Galactic plane, SWIFT J0325.6−0907, which we exclude because it is likely a transient. The source shows a declining significance in the 105-month light curve (Oh et al. 2018),

[38] 838 AGNs + 22 newly identified − 2 DR1 AGNs found to be stellar.

Table 1
New 70-month AGN Counterparts in BASS DR2

BAT ID (1)	Swift Name (2)	Counterpart (3)	R.A. (4)	Decl. (5)	DR2 Type (6)	z (7)	b (8)	A_V (9)
25	SWIFT J0041.0+2444	SWIFT J004039.9+244539	10.1661783	24.7609374	Sy1.9	0.078365	−38.0	0.11
323	SWIFT J0612.2−4645	PMN J0612−4647	93.1121548	−46.788457	BZQ	0.317767	−25.8	0.17
343	SWIFT J0640.0−4737	SWIFT J064013.50−474132.9	100.056201	−47.692985	Sy2	0.057242	−21.5	0.36
359	SWIFT J0709.3−1527	PKS 0706−15	107.302151	−15.450997	BZB	0.142277	−3.2	2.00
364	SWIFT J0714.7−2521	SWIFT J0714.7−2521	108.654098	−25.290303	Sy1	0.042503	−6.5	1.62
367	SWIFT J0723.8−0804	1RXS J072352.4−080623	110.971135	−8.1039597	Sy1.9	0.144926	3.4	0.94
396	SWIFT J0755.4+8402	2MASS J07581638+8356362	119.571766	83.9435807	Sy1	0.133952	28.7	0.15
410	SWIFT J0812.3−4004	1RXS J081215.2−400336	123.058378	−40.05667	Sy1	0.074934	−3.3	5.05
433	SWIFT J0854.3−0827	SWIFT J085429.35−082428.6	133.621953	−8.4076316	Sy2	0.188435	22.6	0.10
494	SWIFT J1020.5−0237A	SDSS J102103.08−023642.6	155.262884	−2.6118136	Sy2	0.293645	43.1	0.13
516	SWIFT J1045.3−6024	2MASS J10445192−6025115	161.216286	−60.419879	Sy2	0.047[a]	−1.3	9.54
761	SWIFT J1512.2−1053A	NVSS J151148−105023	227.952883	−10.840131	BZQ	0.94672	39.0	0.34
780	SWIFT J1548.1−6406	SWIFT J1548.1−6406	237.1265671	−64.0263441	BZQ	1.693124	−7.6	0.64
897	SWIFT J1737.7−5956A	1RXS J173751.2−600408	264.466913	−60.066598	BZQ	3.656025	−14.8	0.23
1000	SWIFT J1852.2+8424A	SWIFT J185024.2+842240	282.60455	84.3790556	Sy1	0.183122	27.0	0.30
1001	SWIFT J1852.2+8424B	1RXS J184642.2+842506	281.707105	84.4181331	Sy1	0.225381	27.1	0.30
1007	SWIFT J1852.8+3002	GALEXASC J185249.68+300425.8	283.206294	30.0741661	Sy1.9	0.057301	12.9	0.62
1075	SWIFT J2024.0−0246	1RXS J202400.8−024527	306.008863	−2.7590708	Sy1.9	0.137523	−21.8	0.21
1083	SWIFT J2034.0−0943	2MASX J20341926−0945586	308.5803195	−9.7664501	Sy2	0.081551	−27.2	0.19
1091	SWIFT J2048.4+3815	1RXS J204826.8+381120	312.112497	38.1903626	Sy1	0.105394	−3.4	2.76
1096	SWIFT J2059.6+4301B	SWIFT J210001.06+430209.6	315.004153	43.036367	Sy2	0.066023	−2.0	4.09
1164	SWIFT J2243.2−4539	2MASX J22422135−4539093	340.588956	−45.652581	Sy2	0.120675	−58.4	0.03

Notes. A detailed description of this table's contents is given in Section 4. Columns (1)–(2): BAT 70-month survey catalog ID and Swift name (https://swift.gsfc.nasa.gov/results/bs70mon/). Column (3): corresponding galaxy counterpart name in NED or SIMBAD based on the WISE positions. Columns (4)–(5): right ascension and decl. of the IR counterpart of the BAT AGN, in decimal degrees, based on WISE positions. Column (6): AGN type based on optical spectroscopy—Sy1 (with broad Hβ), Sy1.9 (narrow Hβ and broad Hα), and Sy2 (with narrow Hβ and Hα). For beamed AGNs, the types include those with the presence of broad lines (BZQ), only host galaxy features lacking broad lines (BZG), or traditional continuum-dominated blazars with no emission lines or host galaxy features (BZB). Column (7): best DR2 redshift measurement and the line or method used for the measurement. Measurements are from a broad-line fitting code (Mejía-Restrepo et al. 2022), when available for all Sy1 and BZQ sources with broad-line Hβ. For narrow-line sources, the redshift is based on emission-line fitting of [O III] λ5007, when possible. For some high Galactic extinction sources or high-redshift sources $z > 1$, other lines are used. Finally, host galaxy templates are used for some continuum-dominated blazars (BZB) with no emission lines. Column (8): Galactic latitude, in decimal degrees. Column (9): visual extinction due to Milky Way foreground dust, using maps of Schlegel et al. (1998) and the extinction law derived by Cardelli et al. (1989).
[a] This particular AGN resides in a region of very high Galactic extinction ($A_V = 9.5$), and the redshift is based on an He II λ10830 line measurement from the literature (Fortin et al. 2018).

with a drop to zero XMM-Newton flux after 2010 January. A 10 ks Swift XRT exposure finds no sources above $F^{\rm obs}_{2-10\ {\rm keV}} = 10^{-13}$ erg cm^{-2} s^{-1} in flux that could be a likely counterpart. No observations of this source have been performed with Chandra, XMM-Newton, or NuSTAR.

2.3. Dual AGNs

In the case of bright dual AGNs, both may contribute significantly to the BAT flux (e.g., Koss et al. 2016b). Dual AGNs are typically close together ($\sim$<30 kpc), show small offsets in redshift (<500 km s^{-1}), and often show signs of interaction in imaging. For these sources, we report them as if they would have been individually detected based on the sky sensitivity (Baumgartner et al. 2013), and we report the fluxes based on the soft X-ray emission (Ricci et al. 2017a). Additional spectra of merging companions (e.g., Koss et al. 2010, 2012) will be presented in a separate release (M. Koss et al. 2022, in preparation).

A summary of bright dual AGNs in the sample can be found in Table 4. This only includes dual AGNs that are both X-ray detected, not lower-luminosity AGNs detected only in optical spectroscopy. The galaxy group Arp 318 (NGC 835/NGC 833) and the close dual AGN Mrk 463 are unique in that the sources are individually below the median BAT sky sensitivity, but the combined flux is above the median sky sensitivity. To be complete, we set the limit at $F^{\rm obs}_{14-195\ {\rm keV}} > 5 \times 10^{-12}$ erg cm^{-2} s^{-1}, which corresponds to the faintest detected sources in the sky by BAT rather than the median sensitivity $F^{\rm obs}_{14-195\ {\rm keV}} > 1.03 \times 10^{-11}$ erg cm^{-2} s^{-1}. We assume $F^{\rm obs}_{14-195\ {\rm keV}} \propto F^{\rm in}_{2-10\ {\rm keV}}$ for this calculation, and $\Gamma = 1.8$, which is consistent at $N_{\rm H} < 10^{23.5}$ cm^{-2} (Koss et al. 2016a; Ricci et al. 2018). This leads to three sets of bright dual BAT-detected AGNs in the DR2. See Ricci et al. (2017a) and Koss et al. (2012) for a further discussion of these sources.

2.4. Weakly Associated AGNs

Previous studies have also found that galaxy clustering is higher around BAT AGNs (e.g., Cappelluti et al. 2010; Koss et al. 2010), and this extends to secondary nearby AGNs on scales of 70–1000 kpc. These AGNs will be separated by significant distances on the sky of several arcminutes, but they show small offsets in redshift (<500 km s^{-1}) and can often be found with several other galaxies clustering at the same redshift. These two AGNs will reside in the BAT beam and may both be bright enough to be individually detected. In other cases, the clustered AGNs would not be individually detected, but they are detected by BAT because of flux boosting. See Section 2.4 for further details on these systems.

Table 2
New Galactic Sources in DR2

BAT ID (1)	Counterpart (2)	R.A. (3)	Decl. (4)	Telescope (5)	b (6)	New Class (7)	70-month (8)	Feature (9)	References (10)
27	CXOM31 J004232.0+411314	10.6336579	41.2206639		−21.6	Pulsar	in M31		Y17
222	SWIFT J042749.42−670436.1	66.9571685	−67.076319	VLT/X-shooter	−38.6	Star		Broad Hα	Ke20
289	SWIFT J053457.91+282837.9	83.7412468	28.4770753		−2.2	CV	on plane		H18
336	WISEA J063033.56+113414.1	97.63994	11.57063		0.8	Star		Broad Hα	
365	1RXS J071748.9−215306	109.4510999	−21.88376786		−4.3	CV	in plane		H18
462	SWIFT J092752.58−694438.8	141.979246	−69.745714		−13.5	CV	SRC/X-RAY		H18
603	1RXS J121324.5−601458	183.3497138	−60.2546853	VLT/X-shooter	2.3	Star		Broad Hα	Ka12
618	XSS J12270−4859	186.994503	−48.895133		13.8	Pulsar	CV?		D15
620	1RXS J123113.2−423524	187.80036	−42.588943	VLT/X-shooter	20.1	Star	X-ray src	Broad Hα	
773	IRAS 15318−5740	234.011699	−57.814826	VLT/X-shooter	−1.7	Star		Ca II Emission	
879	1RXS J172032.0−514414	260.135722	−51.736956	VLT/X-shooter	−8.3	Star	SRC/X-RAY	Ca II Emission	
933	IGR J17507−2856	267.6024	−29.037		−0.9	LMXB	transient		L01
989	SWIFT J183905.82−571507.6	279.774816	−57.251419	VLT/X-shooter	−21	Star	SRC/X-RAY	Ca II Absorption	
993	SWIFT J1842.2−1124	280.5729	−11.4172	Palomar/DBSP	−3.2	LMXB	transient	Ca II Absorption	C16
1061	SWIFT J200622.36+364140.9	301.591132	36.6982992	Palomar/DBSP	2.5	CV	New src	Ca II Absorption	H18
1095	SWIFT J205915.84+430109.5	314.815403	43.0189524	Palomar/DBSP	−1.9	HMXB	SRC/X-RAY	Ca II Absorption	
1159	SWIFT J223703.9+632338	339.155838	63.492667	Palomar/DBSP	4.5	CV	X-ray transient	Broad Hα	H18

Note. Column (1): BAT 70-month survey catalog ID. Column (2): corresponding galaxy counterpart name in NED or SIMBAD based on the WISE positions. Columns (3)–(4): right ascension and decl. of the IR counterpart of the BAT AGN, in decimal degrees, based on WISE positions. Column (5): telescope and instrument used to observe the Galactic source. Column (6): Galactic latitude, in decimal degrees. Column (7): Galactic classification based on reference or optical spectral features. Star denotes stellar features in optical spectrum at redshift zero, but uncertain classification. Column (8): initial classification in 70-month catalog (Baumgartner et al. 2013). Column (9): optical spectral feature used in redshift measurement. Column (10): references.

References. C16: Corral-Santana et al. 2016; D15: de Martino et al. 2015; H18: Halpern et al. 2018; Ka12: Karasev et al. 2012; Ke20: Kennedy et al. 2020; L01: Liu et al. 2001; Y17: Yukita et al. 2017.

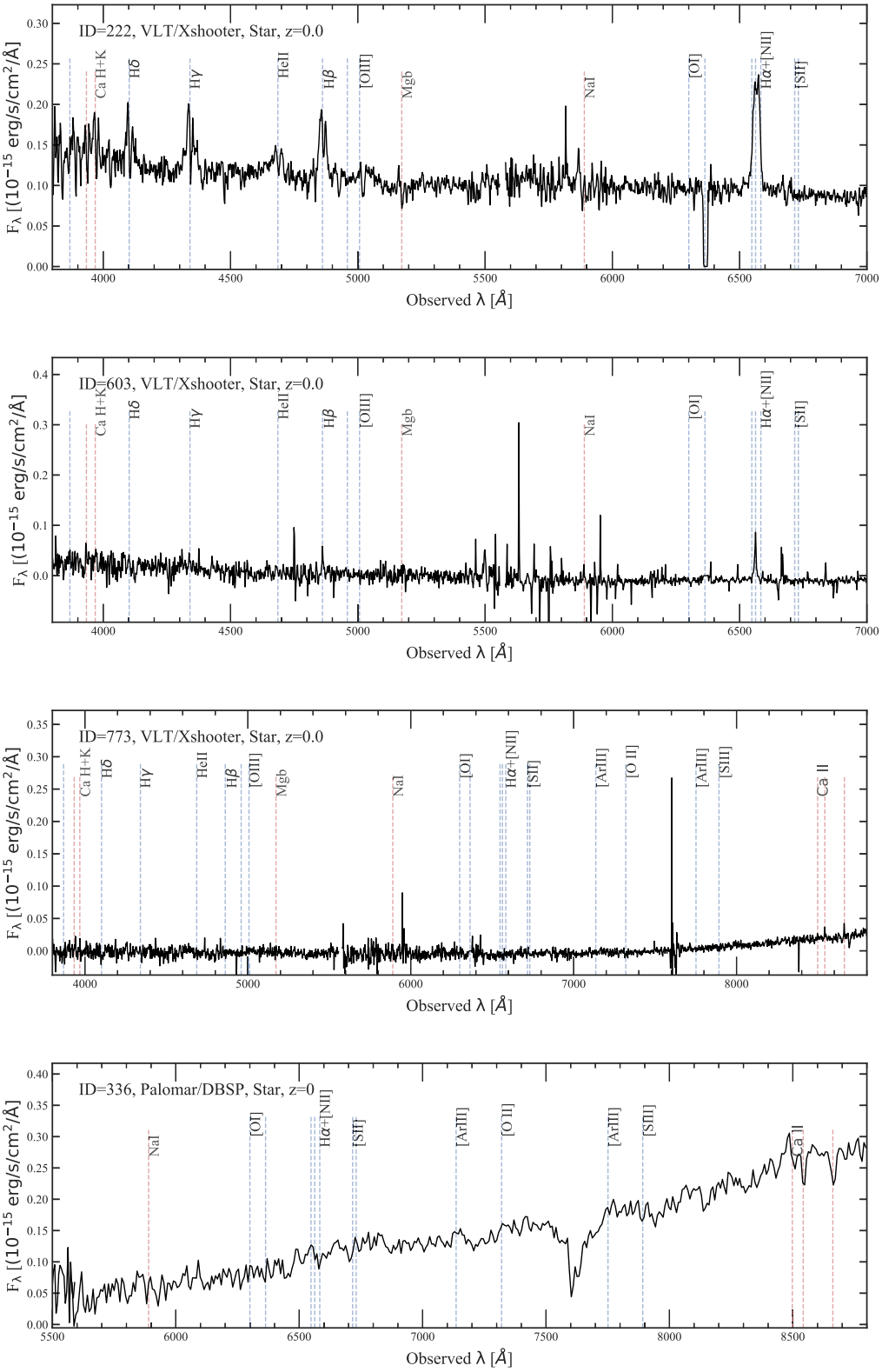

Figure 1. Figure showing spectra of sources identified as Galactic based on emission or absorption lines at redshift zero.

Here we provide a list of multiple soft X-ray AGNs that are detected within the BAT beam but are weakly associated (∼70–700 kpc; Table 5). This includes seven pairs of AGNs. In three cases (SWIFT J0202.4+6824B, SWIFT J0359.0−3015A, SWIFT J1051.2−1704B), one of the AGNs is below the median BAT sky sensitivity and should be excluded from population studies.

2.5. Multiple Unassociated Faint X-Ray Counterparts

Some sources in the initial 70-month catalog were reported with multiple likely counterparts within the error circle of the BAT beam position (Baumgartner et al. 2013). The details of many of these sources and their fluxes were described further in Ricci et al. (2017a) as part of the BASS DR1. Sources

Table 3
Unknown Sources at $|b| < 3°$ and A_V Excluded from DR2

BAT ID	Swift Name	Counterpart	R.A.	Decl.	b	A_V
464	SWIFT J0931.5−5105	SWIFT J093118.1−510845	142.825292	−51.146017	0.20	5.63
706	SWIFT J1403.6−6146	[CG2001] G311.45-0.13	211.12571	−61.789482	−0.13	43.08
742	SWIFT J1447.0−5814	SWIFT J144719.3−581616	221.831011	−58.271689	1.24	7.42
1005	SWIFT J1848.5−0046	IGR J18485−0047	282.106051	−0.7764179	0.32	35.98
1011	SWIFT J1855.5+0516	SWIFT J1855.5+0516	283.92069	5.220055	1.54	21.85
1086	SWIFT J2037.2+4151	SSTSL2 J203705.58+415005.3	309.273359	41.8347872	0.52	20.65
1094	SWIFT J2056.8+4939	RX J2056.6+4940	314.174892	49.6715329	2.76	9.25

Note. Column descriptions are the same as in Table 1, unless otherwise noted.

below the median sky sensitivity ($F^{\rm obs}_{14-195\ {\rm keV}} < 10.3 \times 10^{-12}$ erg cm^{-2} s^{-1}) should be excluded from population studies based on the all-sky sensitivity because they were likely detected only because of X-ray follow-up (Table 6). Among these, 10 pairs of sources 76% (20/26) are cases of flux boosting that individually are below the median sensitivity. Another six cases are fainter counterparts to a brighter BAT source that is above the median detection sensitivity. There is only one case of a pair of AGNs with both AGNs above the detection sensitivity (SWIFT J1652.0−5915), which includes NGC 6221 ($z = 0.0041$) and the background galaxy ESO 138-1 ($z = 0.0091$).

2.6. Beamed and Lensed AGNs

The Swift BAT survey includes beamed, lensed, and unbeamed AGNs, and it is important to separate them in most scientific analyses. The original DR1 included 105 beamed sources (see, e.g., Table 1 of Ricci et al. 2017a), based on the Roma Blazar Catalog (BZCAT) catalog (Massaro et al. 2009) and DR1 optical spectra (Koss et al. 2017). Since this release, a further study by Paliya et al. (2019) used recent Fermi LAT data and SED fitting to identify all the blazars in the 105-month catalog, which includes all DR2 70-month AGNs.

For continuity, we provide all of the new beamed AGNs, or changes of beamed AGNs from the DR1 classifications to unbeamed in DR2 or vice versa, in Table 16 in Section A.1. In most cases, recent radio observations or SED fitting (Paliya et al. 2019) revealed beamed AGNs to be unbeamed, or conversely, a recent Fermi detection revealed a previously categorized unbeamed AGN to be beamed. In DR2, 13/105 (12%) changed from beamed to unbeamed AGN classification. Conversely, eight unbeamed AGNs in the DR1 list were found to be beamed. Finally, five beamed AGNs were included because they are part of the expanded list of AGNs that were not in the original list of 838 DR1 AGNs.

For DR2, we reviewed all the beamed classifications and found three AGNs that were classified as beamed AGNs in Paliya et al. (2019), but we now classify them as unbeamed AGNs based on further analysis. SWIFT J0312.9+4121 (aka QSO B0309+411), while detected in Fermi, is a broad-line radio galaxy with double-lobe morphology within a compact structure (Tzanetakis et al. 1978). For SWIFT J0519.5−3140 (aka PKS 0521−365), Angioni et al. (2019) found with very long baseline interferometry imaging that the jet of PKS 0521−36 is not highly beamed, with viewing angles larger than 10°. Finally, SWIFT J1742.1−6054 (aka PKS 1737−60) was classified as an FR II radio galaxy (Bassani et al. 2016). Further polarimetric observations or detections of compact cores and superluminal motions using high-resolution radio imaging would be needed to further classify these sources.

The beamed DR2 AGNs then total 105, the same as in the DR1 despite the 26 changes. There is also a lensed AGN, SWIFT J1131.9−1233 (aka QSO J1131−1231 at $z = 0.654$), by a galaxy at $z = 0.295$ (Berghea et al. 2017; Sluse et al. 2017). Finally, SWIFT J1833.7−2105 (aka PKS 1830−211 at $z = 2.5$) is both beamed and also lensed (Lidman et al. 1999) by a foreground spiral at $z = 0.89$ (Winn et al. 2002).

3. Survey, Observations, and Data Reduction

Here we provide an overview of DR2 survey and observations. The DR2 targeting criteria goals were to provide the largest possible sample of BH mass measurements from either broad Balmer lines or stellar velocity dispersion measurements, as well as the broadest possible spectral coverage (e.g., 3000–10000 Å) for emission-line measurements for the entire catalog of 858 AGNs. In practice, outside of echelle instruments, this required multiple spectra with broad wavelength coverage with lower resolution or higher-resolution gratings with narrower wavelength coverage. Repeat observations were done if the S/N of the broad Balmer lines (Hβ or Hα) was too low for measurements (Mejía-Restrepo et al. 2022) or the low S/N and/or spectral resolution of the stellar absorption features resulted in a failed measurement of velocity dispersion. We did not reobserve targets with acceptable spectra and measurements from the SDSS. The requirement for high S/N, high spectral resolution, and broad wavelength coverage, combined with queue mode observing approved months in advance, sometimes resulted in duplicate (or more) observations of the same source. Example spectra for different instrumental setups are provided in Appendix B. All spectra associated with DR2 for each AGN will be provided at the BASS website.[39]

A summary of all the observational setups used is shown in Table 7. We did not specifically exclude sources with high Galactic extinction in spectroscopic targeting if there was an obvious optical counterpart to the WISE counterpart of the soft X-ray emission. This resulted in observations of 12 AGNs with very high extinctions (between $A_V = 5$ and 10 mag) close to the Galactic plane ($0 < b < 3°$), primarily to determine the first redshift and AGN type.

The data reduction and analysis of DR2 spectra maintain the uniform approach described in the initial DR1 paper (Koss et al. 2017). All new spectra are processed using the standard tasks for cosmic-ray removal, 1D spectral extraction, wavelength, and flux calibrations, in either IRAF or the ESO/

[39] https://www.bass-survey.com/

Table 4
Dual AGNs in DR2

BAT ID	Swift Name	Primary	Sec.	BAT Total (10^{-12} erg cm^{-2} s^{-1})	Ratio	$F^{\rm obs}_{14-195\ \rm keV}$ Sec. (10^{-12} erg cm^{-2} s^{-1})	Incl.	References
(1)	(2)	(3)	(4)	(5)	(6)	(7)	(8)	(9)
841	SWIFT J1652.9+0223	NGC 6240S	NGC 6240N	72	0.32	23.0	Y	P16
1077	SWIFT J2028.5+2543	MCG +04-48-002	NGC 6921	78	0.20	15.6	Y	K16
112	SWIFT J0209.5−1010	NGC 835	NGC 833	15	0.46	7.1	Y	O18
471	SWIFT J0945.6−1420	NGC 2992	NGC 2993	27	0.14	3.8	N	K12
703	SWIFT J1355.9+1822	Mrk 463E	Mrk 463W	11	0.25	2.7	N	K12
678	SWIFT J1334.8−2328	ESO 509-IG066W	ESO 509-IG066E	18	0.10	1.8	N	Ko17
176	SWIFT J0324.9+4044	IRAS 03219+4031	2MASX J03251221+4042021	19	0.08	1.6	N	K12
1198	SWIFT J2328.9+0328	NGC 7679	NGC 7682	15	0.10	1.5	N	K12
497	SWIFT J1023.5+1952	NGC 3227	NGC 3226	109	0.01	1.1	N	K12
552	SWIFT J1136.0+2132	Mrk 739E	Mrk 739W	13	0.09	1.2	N	K11

Note. Columns (1)–(2): BAT 70-month survey catalog ID and Swift name (https://swift.gsfc.nasa.gov/results/bs70mon/). Columns (3)–(4): primary and secondary galaxy, where the primary galaxy is the one with brighter soft X-ray emission ($F^{\rm in}_{2-10\ \rm keV}$). Column (5): total hard X-ray emission detected from BAT for both sources. Column (6): ratio of the soft X-ray emission of the secondary to the total emission based on intrinsic soft X-ray emission ($F^{\rm in}_{2-10\ \rm keV}$). Column (7): predicted $F^{\rm obs}_{14-195\ \rm keV}$ for the secondary given the soft X-ray emission. Column (8): whether or not the secondary galaxy optical spectra is included in the DR2 release. Column (9): references.

References. Ko17: Kosec et al. 2017; K11: Koss et al. 2011; K12: Koss et al. 2012; O18: Oda et al. 2018; P16: Puccetti et al. 2016.

Table 5
Weakly Associated Counterparts in DR2

BAT ID	Swift ID	R.A.	Decl.	Counterpart	DR2 Type	z	$F^{\rm obs}_{14-195\ \rm keV}$ (10^{-12} erg cm^{-2} s^{-1})	(km s^{-1})	Offset[a] (arcsec)	(kpc)
103	SWIFT J0202.4+6824A	30.5723165	68.3626549	LEDA 89913	Sy2	0.011836	11.53	58	294	72
104	SWIFT J0202.4+6824B	30.384773	68.4060751	LEDA 137972	Sy1.9	0.012028	7.6			
202	SWIFT J0359.0−3015A	59.8354003	−30.20269	SARS059.33488-30.34397	Sy1.9	0.097452	8.42	1086	391	681
203	SWIFT J0359.0−3015B	59.7867976	−30.302943	SARS059.28692-30.44439	Sy2	0.093833	10.98			
520	SWIFT J1051.2−1704A	162.812665	−17.008078	NGC 3431	Sy2	0.01744	22.43	337	529	188
521	SWIFT J1051.2−1704B	162.9061	−17.124721	LEDA 32573	Sy2	0.018563	3.72			
657	SWIFT J1306.4−4025A	196.608846	−40.41461	ESO 323-77	Sy1.5	0.01563	33.06	171	525	168
658	SWIFT J1306.4−4025B	196.800383	−40.407563	ESO 323-81	Sy1	0.0162	16.91			
746	SWIFT J1451.0−5540A	222.888099	−55.677311	LEDA 3079667	Sy1.9	0.018091	40.84	172	1216	461
747	SWIFT J1451.0−5540B	222.303112	−55.605703	LEDA 3085605	Sy2	0.018663	26.5			
754	SWIFT J1506.7+0353A	226.485635	3.7073107	Mrk 1392	Sy1.5	0.036009	19.01	375	905	648
755	SWIFT J1506.7+0353B	226.684	3.862	2MASX J15064412+0351444	Sy2	0.037259	15.67			
1173	SWIFT J2254.2+1147A	343.681327	11.7141072	UGC12243	Sy2	0.028508	12.55	88	428	245
1174	SWIFT J2254.2+1147B	343.581956	11.7825716	UGC12237	Sy2	0.028215	17.11			

Notes. Column descriptions are the same as in Table 1, unless otherwise noted.
[a] Offset between two BAT AGNs in measured redshift (kilometers per second) and WISE position (arcseconds and kiloparsecs) at the redshift of the first AGN listed.

Table 6
Faint Soft X-Ray Counterparts in DR2

BAT ID	Swift ID	R.A.	Decl.	Counterpart	DR2 Type	z	$F^{\rm obs}_{14-150\ \rm keV}$ (10^{-12} erg s^{-1})
29	SWIFT J0042.9+3016A	10.7578514	30.2887771	2MASX J00430184+3017195	Sy2	0.04894	7.72
92	SWIFT J0149.2+2153A	27.2487096	21.7594329	LEDA 1656658	Sy1.9	0.069397	8.69
93	SWIFT J0149.2+2153B	27.353505	21.9973509	NGC 678	Sy2	0.009485	8.17
223	SWIFT J0428.2−6704B	67.4475784	−67.055521	2MASX J04294735−6703205	Sy1.2	0.064848	3.21
320	SWIFT J0609.5−6245A	92.5272683	−62.720088	2MASX J06100652−6243125	Sy1	0.157475	9.45
321	SWIFT J0609.5−6245B	92.1613084	−62.787855	LEDA 2816519	Sy1	0.099173	3.88
494	SWIFT J1020.5−0237A	155.262884	−2.6118136	SDSS J102103.08−023642.6	Sy2	0.293645	6.88
495	SWIFT J1020.5−0237B	154.994136	−2.5767385	SDSS J101958.58−023436.2	Sy1	0.059739	5.93
528	SWIFT J1105.7+5854A	166.495981	58.9460474	Z291-28	Sy2	0.047752	5.89
529	SWIFT J1105.7+5854B	166.406764	58.8557915	2MASX J11053754+5851206	Sy1.2	0.191213	5.34
550	SWIFT J1132.9+1019B	173.247877	10.395067	[HB89] 1130+106	BZQ	0.539603	8.78
554	SWIFT J1138.9+2529A	174.640356	25.3981165	LEDA 1735060	Sy2	0.025363	8.94
555	SWIFT J1138.9+2529B	174.813041	25.5993964	SDSS J113915.13+253557.9	Sy2	0.21925	5.63
601	SWIFT J1213.1+3239B	183.265867	32.7935448	B21210+33	BZQ	2.50706	8.12
632	SWIFT J1240.2+3457A	189.96528	34.9749458	Mrk 653	Sy2	0.042812	9.00
633	SWIFT J1240.2+3457B	190.435624	35.0627157	NGC 4619	Sy1.9	0.022946	7.02
664	SWIFT J1313.6+3650A	198.453989	36.8994443	RX J1313.8+3653	Sy1.5	0.066945	7.12
665	SWIFT J1313.6+3650B	198.364486	36.5938771	NGC 5033	Sy1.9	0.002763	5.52
761	SWIFT J1512.2−1053A	227.952883	−10.840131	NVSS J151148−105023	BZQ	0.94672	5.97
762	SWIFT J1512.2−1053B	228.021112	−10.776578	2MASX J15120505−1046356	Sy2	0.165799	8.31
897	SWIFT J1737.7−5956A	264.466913	−60.066598	1RXS J173751.2−600408	BZQ	3.656025	2.18
924	SWIFT J1747.8+6837A	267.159564	68.7045251	Mrk 507	Sy1.2	0.055038	4.83
925	SWIFT J1747.8+6837B	266.748141	68.6085193	2MASS J17465953+6836303	Sy1.2	0.063785	5.23
1000	SWIFT J1852.2+8424A	282.60455	84.3790556	SWIFT J185024.2+842240	Sy1	0.183122	5.51
1001	SWIFT J1852.2+8424B	281.707105	84.4181331	1RXS J184642.2+842506	Sy1	0.225381	4.19
1096	SWIFT J2059.6+4301B	315.004153	43.036367	SWIFT J210001.06+430209.6	Sy2	0.066023	5.84

Note. Column descriptions are the same as in Table 1.

`Reflex` environment for the Very Large Telescope (VLT) instruments. The spectra are flux-calibrated using standard stars, which were typically observed two to three times per night. The spectra are corrected for Galactic reddening. Finally, a telluric absorption correction is applied to the spectra with the software `molecfit`.

3.1. Master Observing Table

We provide the following key parameters when possible for each individual spectrum (Table 8):

1. `BAT ID`: Catalog ID in the BAT survey.[40]
2. `Telescope, diameter, instrument`: Name of observatory, its diameter, and instrument used.
3. `File and File red`: Name of associated fits spectral file. For telescopes with both a blue and a red side, two spectra are listed.
4. `Flags`: Any associated flags with calibration or spectral extraction. Star: indicates foreground stellar contamination, that a very nearby star ($<2''$) contributed to the emission despite a very small extraction region. Red: indicates that only the red side is extracted because the Galactic extinction was so high (e.g., $A_V > 3$) that no source is detected in the blue. Calibration: indicates that the object was observed under poor conditions or the standard star was observed on a different night, so spectral calibration may be more uncertain than usual. Tellurics: indicates that the spectrum suffers from worse-than-usual telluric correction or that the `molecfit` correction was unsuccessful. Shortblue: the setup has a shorter-than-normal blue wavelength coverage due to a reduction issue.
5. `Date`: UT date of observation.
6. `Spectral Range`: Range of the spectra in angstroms. For telescopes with both a blue and a red side, two spectral ranges are listed with the blue side first.
7. `Grating`: Name of associated grating or grism. If the instrument had both a blue (shorter wavelength) and red camera (longer wavelength), two gratings are listed with the blue side listed first.
8. `R` and `Res FWHM`: Instrumental resolution and FWHM in Å. For telescopes with both a blue and a red side, two numbers are provided with the blue side first.
9. `Slit`: Slit width in arcseconds. For telescopes with both a blue and a red side, two widths are listed with the blue side first.
10. `Slit length`: Extraction length along the slit in arcseconds. For telescopes with both a blue and a red side, two lengths are listed with the blue side first. If multiple exposures were combined with optimal extraction (e.g., Palomar/DBSP), the average value is listed.
11. `Angle`: Position angle in degrees, measured east of north. In most cases the sources were observed at parallactic unless a nearby galaxy was observed in the same slit.
12. `Seeing`: Recorded seeing of observations. When possible we use the average seeing. We have not corrected the seeing observations to the observed air mass.
13. `Exposure`: Total exposure from all combined observations for the individual spectra.

[40] https://swift.gsfc.nasa.gov/results/bs70mon/

Table 7
DR2 Instrument Setups

Telescope	Instrument	Total	Grating (lines mm^{-1})	Range (Å)	Dispersion (Ang pixel^{-1})	Slit Width (arcsec)	Res. FWHM (Å)	R	LSF Type
(1)	(2)	(3)	(4)	(5)	(6)	(7)	(8)	(9)	(10)
Palomar	Doublespec	440	600/316	3150−5598/5200−10500	1.07/1.54	1.5	4.1/4.9	1220/1730	Stars/molecfit
		33				2	4.8/6.5	1040/1290	Sky lines/molecfit
		2				1	3/3.6	1670/2360	Sky lines/molecfit
		1				0.5	2.6/3.2	1920/2660	Sky lines/molecfit
		10	300/316	3413−5500/4760−10500	1.07/1.54	1.5	8.1/4.9	620/1730	Sky lines/molecfit
		10	600/600	3150−5598/5570−8930	1.07/0.82	2	4.8/3.4	1040/2500	Sky lines/molecfit
		6				1.5	4.1/2.8	1220/3030	Sky lines/molecfit
		51	1200/1200	3970−5499/8050−9600	0.55/0.4	2	2.3/1.8	2170/4720	Sky lines/molecfit
		15				1.5	2/1.3	2500/6000	Sky lines/molecfit
VLT	X-shooter	179	Echelle	2990−5560/5337−10200	0.2	1.6/1.5	1.3/1.4	3850/6000	Stars/molecfit
		11				1/0.9	0.9/1.0	5500/8900	Arc lines
		4				1.3/1.2	1.2/1.3	4120/6500	Arc lines
		2				1/1.2	0.9/1.3	5500/6500	Arc lines
		1				0.8/0.7	0.8/0.7	6650/11570	Arc lines/Stars
		36	IFU			1.8	1/0.6	8600/13330	Sky lines
	FORS2	61	600	3400−6100	1.32	1	6	830	Sky lines
		9	300	6100−11000	2.8		6.8	1250	Sky lines
	MUSE	4		4800−9300	1.25	2	2.7/2.7	1850/3150	Instrument
		2				1	2.7/2.7	1850/3150	Instrument
SOAR	Goodman	58	400	4560−8690	0.99/1.98	1.2	5.6/5.2	890/1630	Stars
		9	600	5290−7200	1.29	1.2	3.8	1450	Sky lines
		34	931	8000−9600	0.39/0.78	1.2	2.7	3150	molecfit
		50	1200	7900−9070	0.28	1.2	1.8	4720	molecfit
		2				0.45	0.7	12100	molecfit
APO	SDSS	146	Fiber	3830−9180	1.15/1.96	3	3.0/4.1	1760/2490	Survey
		31		3600−10330		2	2.9/3.4	1650/2070	Survey
du Pont	BC	119	300	3000−9070		1	10.4	480	Stars
Keck	LRIS	15	600/400	3200−5600/5450−10280	1.23/1.19	1	3.9/4.7	1280/1810	Sky lines/molecfit
		4				1.5	4.6/6.3	1090/1490	Sky lines/molecfit
		1	600/600		1.23/0.8	1.5	4.6/5.4	1090/1670	Sky lines/molecfit
		1	600/1200		0.61/0.4	1	3.9/1.6	1280/5310	Sky lines/molecfit
Magellan	MAGE	12	Echelle	3300−10010	0.25	1	1.3	3850	Sky lines

Note. See Section 4 for a detailed description of this table's contents. Column (1): telescope. Column (2): instrument. Column (3): total number of DR2 spectra observed with this setup. Column (4): grating listing the lines per millimeter, if applicable. For instruments with a blue and red side two numbers are listed associated with each grating. Columns (5)–(9): wavelength range (Range), pixel dispersion, resolution (Res.), and resolving power (R). These represent typical values for this setup and may have small differences within individual spectra depending on observing conditions. These quantities may also be wavelength dependent in some cases, and so the values are given at 5000 and 8500 Å depending on the spectral range. Two values are listed when the instrument had both a blue arm and a red arm with different settings. Column (10): method used to determine the instrumental resolution, either with sky lines, with telluric features with `molecfit`, with arc lines, fitting stellar templates to stars, or based on resolutions provided within the survey (e.g., SDSS). The measurements are for 5000 or 8500 Å or both depending on the spectral range. See Section 3.4 for further details.

Table 8
Column Description for the Master Observing Table

Column	Name	Units
1	BAT_ID	
2	Telescope	
3	Diameter	m
4	Instrument	
5	File	
6	File Red	
7	Flags	
8	Date	
9	Range	Å
10	Grating	
11	Grating Red	
12	R	
13	R Red	
14	Res	Å
15	Res Red	Å
16	Slit Width	″
17	Slit Width Red	″
18	Slit Length	″
19	Slit Length Red	″
20	Angle	deg
21	Seeing	″
22	Air mass	
23	Exposure	s
24	CDELT	Å pixel^{-1}
25	CDELT Red	Å pixel^{-1}
26	BC	km s^{-1}
27	EBV	mag

Note. See Section 3.1 for detailed descriptions of each field.

(This table is available in its entirety in machine-readable form.)

14. CDELT: Pixel dispersion in Å pixel^{-1}. For telescopes with both a blue and a red side, two widths are listed with the blue side first. Only included for spectra with linear dispersions (e.g., not the SDSS).
15. Airmass: Average air mass during observation.
16. BC: Barycenter correction in kilometers per second needed for Earth's motion based on observation time and observatory location. The computed correction should be added to any observed velocity to determine the final barycentric radial velocity. As this correction is small (e.g., <30 km s^{-1}), it has not been applied to any catalog measurements in the DR2.
17. EBV: Atmospheric extinction.

We note that all of these observing parameters are not available for every spectrum, including most of the archival sample, but we provide them when possible.

3.2. Overview of Samples

Here we provide a list of the telescopes used and their respective data reductions. A plot of the number of spectra from each telescope is provided (Figure 2), as well as summary plots of typical observing conditions and resolution (Figure 3). The redshift range of observations can be found in Figure 4.

3.2.1. Palomar Telescope

The largest sample of targeted sources, 402, was observed with the Palomar Double Spectrograph (DBSP) on the 200-inch Hale telescope. These AGNs were observed as part of a dedicated program on BAT AGNs (P.I. M. Urry or M. Powell) or as part of the NuSTAR program (P.I. F. Harrison and D. Stern), where they served as backup targets to faint NuSTAR serendipitous sources. The observations were performed between 2012 October and 2020 November. The majority of observations were taken with the D55 dichroic, with the 600/4000 and 316/7500 gratings using a 1.″5 slit. This setup provided resolutions of ∼4.4 Å and ∼5.8 Å FWHM, over the ∼3150–5650 Å (blue) and ∼5400–10500 Å (red) regions, respectively, providing full spectroscopic coverage of the optical region. The size of the aperture used for extraction along the slit depended on the specific observing run but was either fixed at 1.″5–2″ or matched to the extended profile of the source in the IRAF APALL task. We note that there are some flux calibration issues at some of the grating edges due to loss of sensitivity specifically at 5400–5650 Å on the blue side and 5400–5600 Å on the red side and at 10000–10500 Å (see examples in Appendix B). In some cases, the region between 5400 and 5650 Å was not extracted. In addition, we did not force the spectra to be flux-calibrated in the overlapping regions, and differences of 10%–20% in flux may occur between the blue and red sides.

A smaller set of 66 narrow-line AGNs and Sy1.9 AGNs were also observed using the higher-resolution 1200 line mm^{-1} grating for higher spectral resolution velocity dispersion measurements of the 3960–5500 Å and 8150–9600 Å regions, respectively.

3.2.2. Very Large Telescope

A total of 211 were observed with X-shooter, a multi-wavelength (3000–25000 Å) echelle spectrograph with medium spectral resolution $R = 4000$–18,000 (Vernet et al. 2011). Two dichroics are used to split the incoming light into the three arms for efficient observation of all three arms simultaneously. The UVB arm (3000–5595 Å), VIS arm (5595–10240 Å), and NIR arm were used (10240–24800 Å). In some cases the NIR range only extended to 21010 Å rather than 24800 Å. More information on the NIR reductions and scientific results can be found in den Brok et al. (2022).

The majority of observations were observed with 1.″6 and 1.″5 in the UVB and VIS arms, respectively, in the NODDING mode and extracted with a 4″ aperture along the slit. The focus of the program was on obscured AGNs (e.g., Sy1.9 and Sy2) to use the broad wavelength coverage and high spectral resolution to measure BH masses from velocity dispersion. These observations were performed as part of a filler program sometimes during bad weather conditions; however, the median seeing was still 1.″02 owing to the inherently good conditions at the VLT. In the case of VLT/X-shooter the spectra were first reduced using the standard pipeline in the ESO reflex software (v2.3.0; Freudling et al. 2013).

Another 19 sources were observed as part of the LLAMA sample (Davies et al. 2015) of low-redshift, luminous BAT AGNs ($z < 0.01$). These sources were observed in the IFU-offset mode with a field of view (FOV) of 1.″8 × 4″ with resolution $R \sim 8400$ and $R \sim 13200$ in the UVB and VIS arms, respectively. The spectra were reduced using the ESO X-shooter pipeline v2.6.0. The spectra were corrected for telluric absorption using telluric standard stars. A more detailed description of the VLT/X-shooter data processing is given in Burtscher et al. (2021).

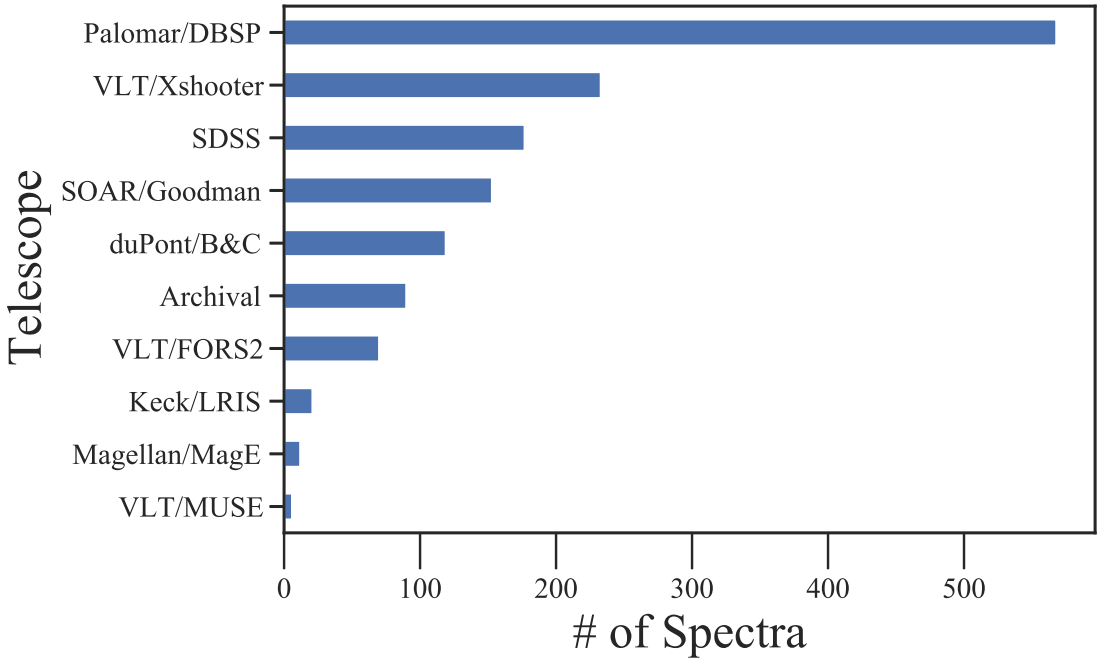

Figure 2. Horizontal bar chart showing the number of spectra taken with each telescope, instrument, or survey. The archival sample is from earlier surveys that were not included in the DR1, including ROSAT AGNs that overlap with BASS in unpublished or published (Grupe et al. 2004) works, from the Palermo surveys of Swift BAT AGNs (Rojas et al. 2017), or as part of an atlas of low-redshift AGNs (Ho & Kim 2009).

Finally, three spectra were part of the Science Verification data from VLT/X-shooter in 2009 and lack header information necessary to be processed in the standard way using ESO/Reflex. Two of these spectra, obtained in the SLIT, NODDING mode, were processed using optimal extraction and telluric standard stars following the reductions procedure of Becker et al. (2019). The UVB arm was binned to 15 km s^{-1} pixels. VIS and NIR arms were binned to 10 km s^{-1}. A final IFU spectrum of NGC 7319 was extracted with a $4'' \times 2''$ region following the LLAMA sample.

There were also 69 observations with VLT/FORS2 done in a single observing semester in 2017 (099.A-0403A) and were focused on Sy1 or Sy1.9 AGNs. For FORS2, the majority were observed with the 600B grating, with $1''$ slit, covering 3400–6100 Å. A smaller subset of higher-redshift sources ($z > 0.8$) was done with the 300I grating covering 6100–11000 Å. All sources were reduced with v5.3.32 of the pipeline. Optimal extraction was used with typical extractions along the slit of $9''$.

3.2.3. Southern Astrophysical Research Telescope

We observed 153 sources at the Southern Astrophysical Research (SOAR) telescope using the Goodman instrument as part of six programs between 2017 and 2020 (P.I. C. Ricci). Observations were acquired in two lower-resolution setups focused on unobscured AGNs with the 400 line mm^{-1} grating and GG455 blocking filter or 600 line mm^{-1} grating and GG385 blocking filter. We performed higher-resolution observations of obscured sources focused on the calcium triplet (CaT: 8498, 8542, and 8662 Å) using the 930 line mm^{-1} or 1200 line mm^{-1} grating. Nearly all observations were done with a $1\farcs2$ slit, with just two sources done with a $0\farcs45$ slit, because of the very low velocity dispersions. All sources were extracted optimally, with typically slit lengths of $4\farcs8$.

3.2.4. Du Pont Telescope

Over 11 nights in 2016, 119 AGNs were observed with the du Pont telescope with the Bollens & Chivens spectrograph (P. I. C. Ricci). All sources were observed with a $1''$ slit, the 300 line mm^{-1} grating covering 3000–9070 Å. The sources were extracted with an optimal extraction with typical lengths along the slit of $6\farcs6$. The sources were typically unobscured AGNs, due to the relatively low resolution (FWHM $\sim$ 8.7 Å).

3.2.5. Keck Telescope

Some AGNs were also observed with the Keck telescopes associated with observations of NuSTAR-observed AGNs and mergers (e.g., Koss et al. 2016b). A total of 21 observations were carried out using the Low Resolution Imaging Spectrometer (LRIS; Oke et al. 1995) on the Keck I Telescope. The setup used the blue (600 line mm^{-1}) grism and the red (400 line mm^{-1}) grating, with the D560 dichroic. The majority of observations were done with a $1''$ slit, with a handful done with a $1\farcs5$ slit.

3.2.6. Magellan Telescope

We performed 12 observations with the Magellan Echellete (MagE) spectrograph (Marshall et al. 2008) on the Magellan Clay telescope. We used a $1''$ slit for observations with the slit angle set to parallactic. The data were processed with the magE pipeline, which is part of the Carnegie Python Distribution (`CarPy`, v1.4.2). The wavelength coverage was $\sim$3300–10000 Å, though there was significant detector fringing above 8280 Å, resulting in strong instrumental issues above this range. Typical exposure time was 1 hr and targeted higher-redshift type Sy1.9 and Sy2 AGNs ($z > 0.08$) for velocity dispersion measurements.

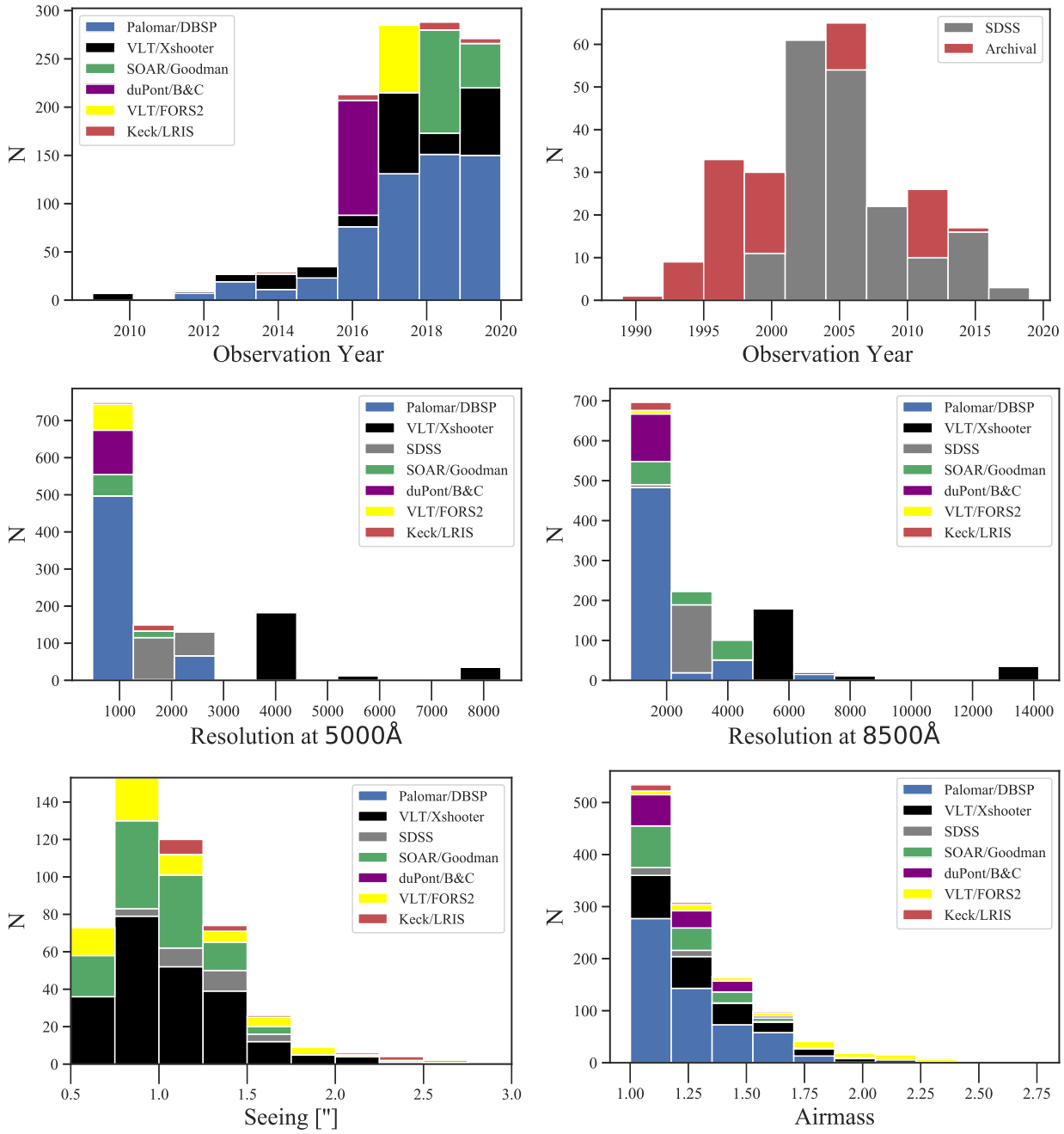

Figure 3. Summary of the different observing conditions for DR2 spectra for telescopes with more than 15 spectra. Observing dates are shown for the newly observed sample (top left) and archival sample (top right). The spectral resolution at 5000 Å (middle left) and 8500 Å (middle right) for the different observations. Finally, the seeing and average air mass of the observations (bottom row).

3.2.7. SDSS and Archival Data

We also included additional spectra from archival sources. We used spectra from the SDSS (York et al. 2000), with 151 sources from data release 16 (DR16; Ahumada et al. 2020), which were observed in the legacy survey with 3″ fiber at ∼3800–9200 Å coverage or 2″ fiber from BOSS or eBOSS with ∼3600–10200 Å coverage, respectively.

We also include 90 additional archival spectra of AGNs that were acquired after the DR1. These include AGNs observed with earlier surveys of ROSAT AGNs that overlap with BASS of unpublished and published (Grupe et al. 2004) sources, from the Palermo surveys of Swift BAT AGNs (Rojas et al. 2017), or as part of an atlas of low-redshift AGNs (Ho & Kim 2009).

Finally, we include six archival spectra from VLT/MUSE when our existing BASS spectra were insufficient. This includes the nearby Circinus galaxy and NGC 3393, which was too bright to observe using our standard setups and was not part of the DR1 archival sample. In addition, the dual AGNs NGC 6240N and NGC 6240S have VLT/MUSE spectra for each AGN obtained in adaptive optics (AO) mode owing to their close separation. Finally, the relatively distant Sy2 sources, BAT ID 1204 ($z = 0.6$) and ID 209 (at $z = 0.09$), were included in order to enable velocity dispersion measurements. We use the processed data from the ESO Science

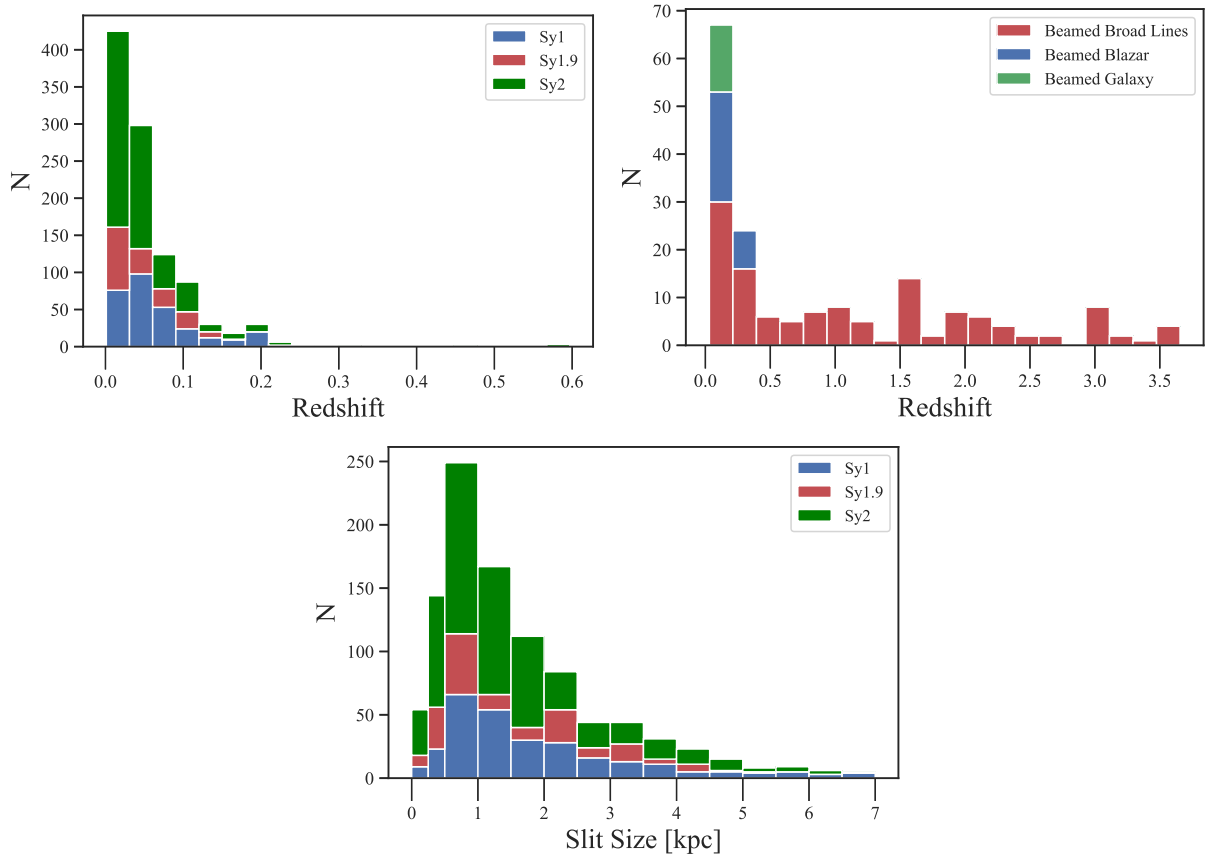

Figure 4. Redshift range of all the AGNs in the sample, split into unbeamed (top left) and beamed AGNs (top right). Additionally, the bottom panel shows the slit width size in kiloparsecs for all the unbeamed AGNs.

archive. We extract a 2″-radius aperture at the WISE position, except for NGC 6240N and NGC 6240S, for which we use a 1″-radius aperture owing to their closeness.

3.3. Telluric Absorption Correction

In DR2 we have implemented the software `molecfit` (Smette et al. 2015) to correct telluric absorption regions that affect the measurements of emission and absorption lines. This includes the oxygen bands (the A, B, and the weaker Γ bands at $\sim 7590 < \lambda/\text{Å} < 7720$, $\sim 6860 < \lambda/\text{Å} < 6950$, and $\sim 6280 < \lambda/\text{Å} < 6340$, respectively), as well as water vapor bands ($\sim 8100 < \lambda/\text{Å} < 8300$, $\sim 8930 < \lambda/\text{Å} < 9800$). The performance has been described already in detail in Kausch et al. (2015) and Smette et al. (2015) for ESO instruments.

In `molecfit`, model spectra are fitted to the observed spectra to derive the best-fit atmospheric parameters by iteratively computing transmission curves using a simple Earth atmosphere structure at the time of observation. Global weather data are combined with local weather data to provide a likely best fit (humidity, pressure, temperature). We use four regions with strong atmospheric features (O_2 at $\sim 6800 < \lambda/\text{Å} < 6900$, O_2 at $\sim 7460 < \lambda/\text{Å} < 7560$, telluric regions at $\sim 9100 < \lambda/\text{Å} < 9200$, and telluric regions at $\sim 9400 < \lambda/\text{Å} < 9500$) to determine the best-fit atmospheric parameters. An example is provided in Figure 5. We mask regions with strong AGN emission-line features from the fitting. We use a Gaussian kernel variable with wavelength (`varkern` = 1).

Telluric corrections with `molecfit` were applied to all spectra with coverage above 7500 Å except archival observations (which lacked local weather data), Magellan/MAGE observations (because of significant fringing), and SDSS spectra (which have already had this correction applied). An example of the telluric correction and its importance for narrow- and broad-line measurements is provided in Figure 6. We note that the ability to recover the intrinsic spectra is dependent on the ability to measure foreground atmospheric absorption lines in the source, and thus very faint intrinsic spectra, such as those with very high Galactic extinction, have little or no correction. While most spectroscopic regions were adequately corrected, the 9300–9700 Å region suffers very high extinction, and emission-line fitting should be approached with caution.

3.3.1. Overlap with the DR1

Initial targeting priority focused on sources without BH mass measurements or spectra from the archival data in the DR1, but this was later expanded to complete the whole sample. The DR2 includes all of the SDSS spectra in the DR1, as well as 35 early Palomar spectra that were reprocessed to include corrections with `molecfit`. Beyond this there are still 42 AGNs in the DR1, with no new DR2 spectra.

3.4. Instrumental Resolution

We determine the instrumental resolution and line-spread function (LSF) FWHM for each spectral setup and provide the best estimate in Table 7. A description of how this quantity was measured is given in Section 3.4.

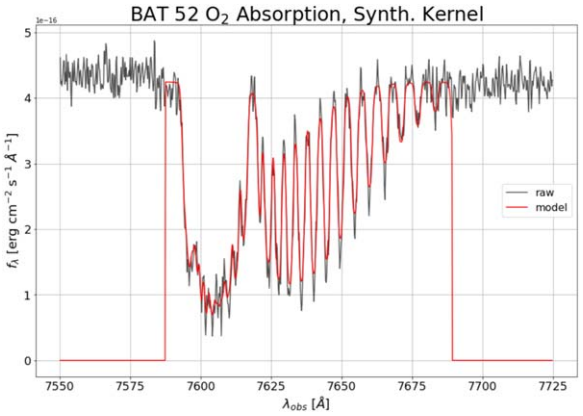

Figure 5. Example absorption-line fit of the model spectrum to the observed spectrum using synthetic kernels of Gaussian kernels in the O_2 A-band region (∼7580–7680 Å).

For some sources we perform Gaussian fits of night-sky lines including Hg I (e.g., 4046, 4358, and 5461 Å) and O I (5577, 6300, and 6364 Å) for bluer spectral regions. We used OH lines for redder regions (e.g., 6864, 7341, 7821, and 9872 Å). If this was not feasible owing to spectral coverage, we used arc line spectra.

In real observations, the slit width is not the only factor in determining the instrumental resolution. If the slit is large, the image quality at the entrance slit can be smaller than the slit width. The observed spectral resolution is then better than what is measured from the slit width for arc or sky lines that fully fill the slit, but it is instead determined by the sharpness of the image of the object at the entrance slit. Thus, the spectral resolution in real observations of AGNs may be somewhat smaller than when measured using sky lines or arc line spectra that fully fill the slit.

The measurements from `molecfit`, which trace the absorption of telluric lines, can provide an additional estimate of the effective resolution. We note, however, that the ability to fit the absorption profile is difficult in faint sources and only done for setups that include coverage of telluric features (e.g., >9000 Å). In several setups without telluric features, only a few AGNs were observed, and we use sky or arc lines for resolution measurements.

An independent estimate of the spectral resolution and the line spread was also done with the penalized PiXel-Fitting method (`pPXF`; Cappellari & Emsellem 2004; Cappellari 2017) by fitting stellar absorption lines to individual Galactic stars that were observed during the observations. We use two template libraries depending on the resolution. We use the X-shooter data release 2 library, which was obtained at much higher resolutions than typical observations (e.g., $R \sim 10{,}000$). For spectra obtained at higher resolutions ($R > 3000$) based on sky lines, we use the `PHOENIX` theoretical spectral library (Husser et al. 2013) as a template, which has much higher resolutions ($R \sim 500{,}000$). We fit the 3880–5500 Å region and 8350–8730 Å region to determine the LSF in the blue and red ranges, respectively, to target stellar absorption features.

We find that the spectral resolution as measured from individual Galactic stars during real observations or telluric absorption lines in the AGN galaxies tends to indicate spectral resolutions somewhat sharper (∼20%) than those of sky lines. For instance, for the largest sample observed using the 1.″5 slit with Palomar/Doublespec, the average of stars observed on different nights is 4.7 ± 0.3 Å in the CaT, compared to the average of the telluric absorption with `molecfit`, which is 4.9 ± 0.6 Å. The average from fitting sky lines for these observations is 5.8 ± 0.3 Å. In this case, we use use the `molecfit` average, though it is statistically similar to that from stars. For the 3880–5500 Å region, `molecfit` was not used because of a lack of telluric features, but the `pPXF` fits were 4.1 ± 0.2 Å versus 4.8 ± 0.4 Å for the sky lines within each observation, and the average of the `pPXF` fits was used.

4. Survey Measurements

The spectroscopic release provides spectra for 95.1% (816/858) of DR2 AGNs. When combined with the DR1 spectra, all AGNs have spectra (e.g., 100%, 858/858), representing a complete census of luminous hard-X-ray-selected AGNs over nearly the entire sky outside of a small region on the Galactic plane (94.8%, $|b| > 3°$). Here we describe the main survey measurements (e.g., z, AGN type, $M_{\rm BH}$). Further derived measurements (broad-line widths, narrow-line widths, velocity dispersions) will be provided in subsequent papers.

For all the AGNs in our sample, we provide the following key parameters when possible for each AGN in Table 9:

1. `BAT ID`: Catalog ID in the BAT survey.[40]
2. R.A. $\alpha_{\rm J2000}$ and decl. $\delta_{\rm J2000}$: R.A. and decl. of the optical/IR counterpart of the BAT AGNs, in decimal degrees, based on WISE positions.
3. `DR2 Type`: AGN type based on optical spectroscopy. Sy1 (with broad Hβ), Sy1.9 (narrow Hβ and broad Hα), and Sy2 (with narrow Hβ and Hα). For beamed AGNs, the types include those with the presence of broad lines (BZQ), only host galaxy features lacking broad lines (BZG), or traditional continuum-dominated blazars with no emission lines or host galaxy features (BZB). BZU refers to a beamed AGN where the type is uncertain because of a lack of optical spectroscopy or very low S/N.
4. z and $z_{\rm type}$: Best DR2 redshift measurement and the line or method used for the measurement. The majority of fits are done with [O III] λ5007 (88%, 755/858). Measurements are from a broad-line fitting code (Mejía-Restrepo et al. 2022) referred to as OIII broad, MgII broad, and CIV broad, respectively, when available for all Sy1 and BZQ sources with broad-line Hβ. For narrow-line sources, the redshift is based on emission-line fitting of [O III] λ5007, when possible. For some high Galactic extinction sources, single emission-line fits to other lines are used (in the table as Ha for Hα, SIII for [S II] λ9531, and HeI for He II λ10830). For some high-redshift sources $z > 1$ without high-quality broad-line fitting we report the estimates from single emission-line fits of C IV λ1549 and Mg II λ2798 (referred to as CIV and MgII). Host galaxy templates (referred to as Gal Temp) are used for some BZB with no emission lines. For the remaining sources, DR1 fits or those from SIMBAD are used for redshift estimates.
5. `Dist` and $z_{\rm ind}$: Distance assumed based on redshift or redshift-independent distance measurements in megaparsecs.
6. `Best MBH` and $\rm MBH_{Meth}$. The best BH mass measurement and the method used for the measurement. We do not report errors from either broad-line fitting or velocity

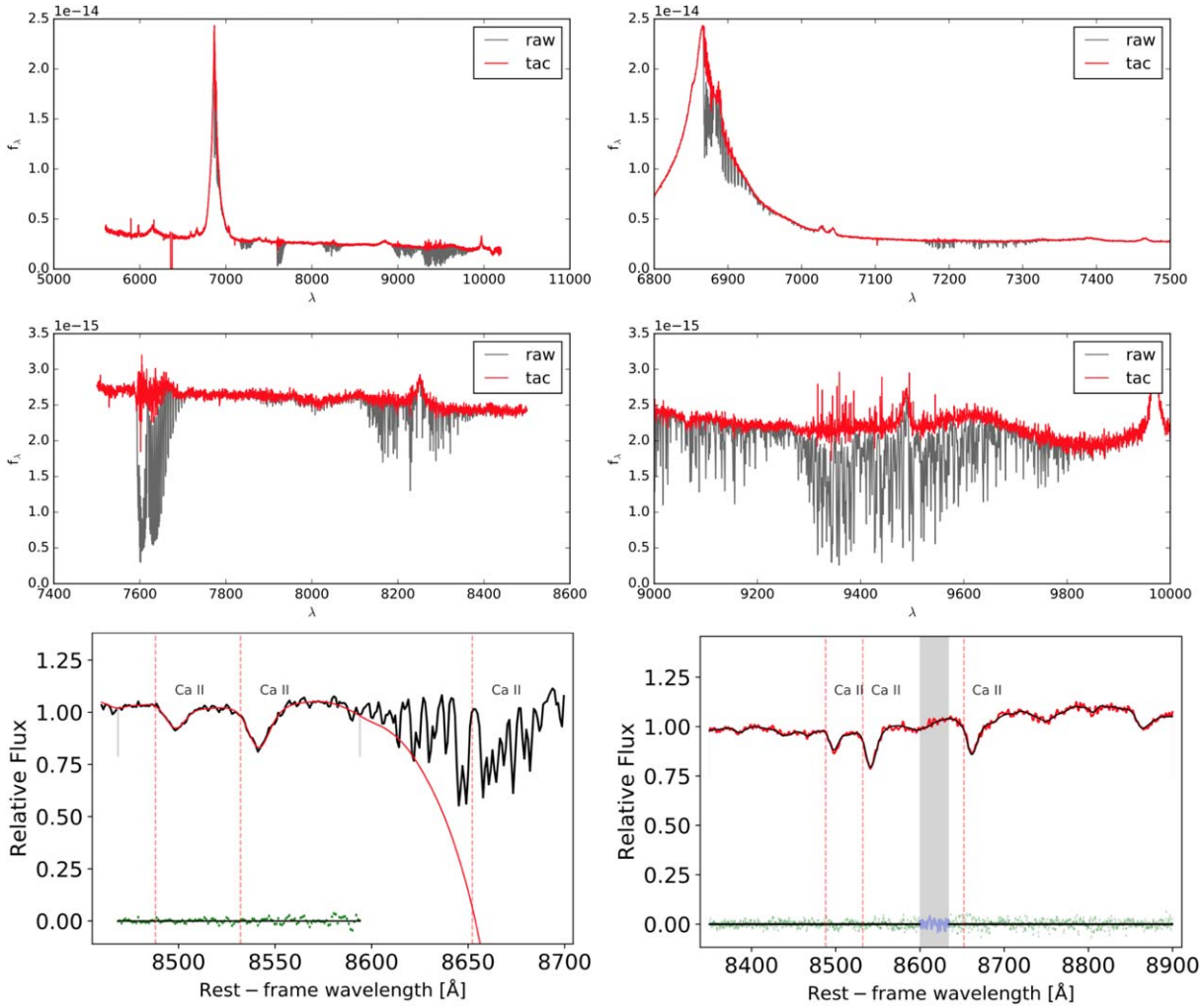

Figure 6. Figure showing `molecfit` correction on a spectrum within the BASS DR2. Top left: VLT/X-shooter spectra of a broad-line BAT AGN Fairall 9 in the visual arm (5500–10500 Å). The top right panel and middle row show zoom-in regions around absorption features. The red lines are the telluric-absorption-corrected (TAC) spectra, and gray lines are the input raw spectra. The telluric absorption features cover broad Hα, as well as the prominent narrow emission lines at He II λ8237 and [S II] λ9531 emission lines. `molecfit` recovers these emission lines as shown with the TAC spectra, which are particularly important for accurately measuring Hα, He II λ8237, and [S II] λ9531. The bottom row shows the CaT region before (left) and after (right) `molecfit` correction when being fit with a galaxy template for a velocity dispersion measurement (Koss et al. 2022b). The model fit is shown in red, with residuals from the fit shown with green dots below the spectra. The TAC spectrum is able to recover a larger region of the Ca II triplet spectral region (8450–8700 Å), which is redshifted into telluric features at $z > 0.04$ with no significant increase in residuals.

dispersions, as they are less than 0.1 dex and the errors are dominated by the intrinsic spread of virial and $\sigma_\star$-based BH mass estimates of order 0.5 dex (Ricci et al. 2022).

7. $L_{\rm bol}$ and $L/L_{\rm Edd}$: Measurement of the AGN bolometric luminosity and Eddington ratio based on BH mass.

4.1. AGN Type

For classification, we first split the sources into 752 unbeamed AGNs and 105 beamed AGNs (and 1 lensed AGN) following the spectroscopic classification of the Roma Blazar Catalog (BZCAT; Massaro et al. 2009). The beamed AGNs were split into three categories based on their optical spectral properties, specifically, based on the presence of broad lines (BZQ), only host galaxy features lacking broad lines (BZG), or traditional continuum-dominated blazars with no emission lines or host galaxy features (BZB).

Overall 72/105 (69%) of the DR1 beamed AGNs maintained the same classification with further optical spectroscopic study. A total of 20/105 (19%) changed specific beamed AGN classification based on additional DR2 optical spectra (e.g., BZG to BZQ, based on the detection of broad Hβ or any other broad line such as Hα).

We provide an unbeamed AGN type based on the presence of broad Balmer lines from visual inspection after fitting with host galaxy templates (Koss et al. 2022b). These include sources with broad Hβ (Sy1), sources with narrow Hβ but broad Hα (Sy1.9), and sources with only narrow optical lines (Sy2). Further classification of broad-line AGNs (e.g., Sy1.2, Sy1.5, Sy1.8, etc.) is provided in subsequent studies (Mejía-Restrepo et al. 2022) and also of narrow-line AGNs such as LINERs (Oh et al. 2022). When spectra are not available in DR2 for AGN type, we use the DR1 AGN type.

Overall, there are 168 AGNs in DR2 for which we derive a revised or first classification of AGN type based on our

Table 9
General AGN Properties

BAT ID	Counterpart	R.A. (deg)	Decl. (deg)	DR2 Type	z	$z_{\rm type}$	Dist (Mpc)	$M_{\rm BH}$ ($M_\odot$)	BH Meth.	log $L_{\rm bol}$ log(erg s^{-1})	$L/L_{\rm Edd}$
1	2MASX J00004876−0709117	0.203234	−7.153223	Sy1.9	0.037496	OIII	165.2	7.61	Vdisp	44.45	−1.33
2	2MASX J00014596−7657144	0.442035	−76.953963	Sy1	0.058505	OIII Broad	261.7	7.41	Hb	44.77	−0.82
3	NGC 7811	0.610105	3.351912	Sy1	0.025457	OIII Broad	111.2	6.70	Hb	44.01	−0.86
4	2MASX J00032742+2739173	0.864248	27.654725	Sy2	0.039784	OIII	175.6	7.89	Vdisp	44.52	−1.55
5	2MASX J00040192+7019185	1.008241	70.321752	Sy2	0.095681	OIII	439.1	6.20	Ha obs	45.29	0.92
6	Mrk 335	1.581400	20.202951	Sy1	0.025906	OIII Broad	113.2	7.23	Lit	44.24	−1.17
7	SDSS J000911.57−003654.7	2.298335	−0.615222	Sy2	0.073345	OIII	331.5	8.54	Vdisp	45.05	−1.67
8	Mrk 1501	2.629175	10.974862	BZQ	0.089385	OIII Broad	408.5	8.07	Lit	45.63	−0.61
9	[HB89] 0014+813	4.285420	81.585596	BZQ	3.377817	CIV Broad	29310.9	9.90	CIV	48.90	0.82
10	LEDA 1348	5.281408	−19.168191	Sy1.9	0.095846	OIII	439.9	8.94	Vdisp	45.41	−1.70
13	LEDA 136991	6.385030	68.362439	Sy2	0.012492	OIII	54.0	7.68	Vdisp	43.94	−1.92
14	LEDA 433346	6.669470	−53.163275	Sy1	0.063219	OIII Broad	283.7	8.44	Hb	44.99	−1.63
16	PG 0026+129	7.307096	13.267761	Sy1	0.141997	OIII Broad	671.7	8.49	Lit	45.68	−0.98
17	ESO 112-6	7.682626	−59.007215	Sy2	0.029004	OIII	127.0	7.90	Vdisp	44.44	−1.64
18	2MASX J00331831+6127433	8.326442	61.462015	Sy1.9	0.104184	OIII	480.9	7.95	Ha	45.42	−0.71
19	RHS3	8.570040	−79.088963	Sy1	0.074268	OIII Broad	335.9	8.02	Hb	44.79	−1.41
20	2MASX J00343284-0424117	8.636619	−4.403423	Sy2	0.212982	OIII	1051.6	9.22	Vdisp	46.22	−1.18
22	Z535-12	9.087263	45.664900	Sy1	0.047608	OIII Broad	211.3	7.36	Hb	44.75	−0.79
24	Mrk 344	9.633812	23.613408	Sy2	0.025246	OIII	110.2	7.54	Vdisp	44.29	−1.43
25	SWIFT J004039.9+244539	10.166178	24.760937	Sy1.9	0.078365	OIII	355.4	7.73	Vdisp	44.86	−1.05
28	NGC 235A	10.720042	−23.541046	Sy1.9	0.022065	DR1	96.1	8.49	Vdisp	44.61	−2.06
30	2MASX J00423991+3017515	10.666287	30.297621	BZQ	0.140128	OIII Broad	662.1	8.56	Hb	45.41	−1.33

Note. Table 9 is published in its entirety in the machine-readable format for 858 AGNs. A portion is shown here for guidance regarding its form and content. See Section 3.1 for a description of each data column.
(This table is available in its entirety in machine-readable form.)

Table 10
Summary of Redshift Measurements

Redshift Method	Count
[O III] λ5007	393
[O III] λ5007 Broad	364
DR1	34
Gal Temp	22
C IV λ1549 Broad	13
Mg II λ2798 Broad	10
Hα	7
SIMBAD	6
C IV λ1549	3
[S II] λ9531	3
He II λ10830	1
NED	1
None	1

Note. The [O III] broad redshift indicates that a broad-line fitting procedure for Hβ was used as described in Mejía-Restrepo et al. (2022). Otherwise, a single emission-line fit or a galaxy template fit was performed. See Section 4.2 for details.

measurements. A detailed comparison of DR2 measurements compared to the DR1 is provided in Appendix A.

4.2. Redshifts

To determine the best redshifts for the sample (Table 10), we use the [O III] λ5007 line emission as the primary measurement. For broad-line sources (e.g., Sy1 and BZQ), the [O III] redshift is based on the fitting procedure in Mejía-Restrepo et al. (2022), which is consistent with the procedure used in the DR1. For more distant beamed AGNs, when the [O III] λ5007 line is redshifted out of the spectrum, the Mg II λ2798 ($0.8 < z < 2.6$) or C IV λ1549 ($2.1 < z < 3.6$) line is used.

For the Sy1.9 and Sy2 AGNs, or any broad-line AGN where the fitting failed, we fit the [O III] emission line in our sample using `PySpecKit`, an extensive spectroscopic analysis toolkit for astronomy, which uses a Levenberg–Marquardt algorithm for spectral fitting (Ginsburg & Mirocha 2011). We fit the [O III] emission line using a single Gaussian. Finally, for 10 sources that are highly reddened and often in the Galactic plane where an [O III] line was not detected we use the Hα or [S II] $\lambda\lambda$6717, 6731 or He II λ10830 line. We note that for NGC 6240N and NGC 6240S the sources were too close together to resolve in our spectra, so we provide a single measurement.

There are 30 beamed AGNs that are strongly continuum-dominated blazars (BZB), with only weak stellar features, and host-galaxy-dominated blazars (BZG), where no [O III] λ5007 emission lines are measured. For 25 of these sources, we can measure redshifts using `pPXF` with the Ca H and K lines or Ca II absorption features. Further details, including a full list of redshifts from stellar absorption features from galaxy template fits for Sy1.9 and Sy2 AGNs, can be found in Koss et al. (2022b).

We used the BASS DR1 data for the 33 AGNs in DR2, which did not have a new spectrum at all or were missing one that covered the [O III] λ5007 line.

For the remaining sources we rely on NED or SIMBAD or past publications for redshift measurements. Of the remaining six BZB sources for which we could not detect strong host galaxy features for a redshift, there are five sources with an existing redshift from NED or SIMBAD, which we use as the redshift measurement. There is one very high extinction AGN ($A_V = 9.5$), 2MASS J10445192–6025115, which was found to have a redshift of $z = 0.047$ (Fortin et al. 2018) based on the He II λ10830 line. The beamed and lensed AGN PKS 1830–21 was measured using Hα in the NIR at $z = 2.507$ (Lidman et al. 1999) owing to its high extinction (A_V) from being in the Galactic plane.

Overall the redshift completion is extremely high, 99.8% (857/858), for the full sample. Of these AGN redshifts, 47 (Table 11) are found for the first time (Figure 7). The only AGN without a redshift is a continuum-dominated blazar (BZB). The blazar, B3 0133+388, was first discovered in the third Bologna sky survey of 408 MHz radio objects (Ficarra et al. 1985) and also shows bright gamma-ray emission above 1 GeV in Fermi. The source shows faint Ca H and K lines at redshift zero in two different Palomar spectra (and also in a Keck/LRIS spectrum shown in Aliu et al. 2012). However, given the radio and Fermi detection, the source is unlikely to be Galactic but may be a blazar with a foreground star.

4.3. Distance and Luminosity

The AGN host galaxies span a large range of redshifts down to very nearby (<50 Mpc) systems. These AGNs can have substantial peculiar velocities compared to velocities of the Hubble flow where a simple assumption of uniform expansion would lead to large errors. High-quality redshift-independent distances to nearby galaxies such as through using the tip of the red giant branch (TRGB) are now available (e.g., McQuinn et al. 2017). Further compilations such as the Extragalactic Distance Database (EDD, Tully et al. 2009) or the Cosmicflows-3 project (Courtois et al. 2017) have now compiled motions of many thousands of local galaxies.

We follow the approach of Leroy et al. (2019), which performed a careful analysis of which compilations to adopt at different distances based on statistical uncertainties. Specifically, we limit our search to <50 Mpc (or 3500 km s^{-1}) galaxies to adopt redshift-independent distances, as beyond this the typical uncertainties are larger than those in the Hubble flow. We focus on using EDD, Cosmicflows, and NED for adopting distances. We adopt a TRGB and "quality" distances from EDD whenever available. When this is not available, we take the Cosmicflows-3 value. If none of these are available, we use the most recent redshift-independent estimate from NED. This results in redshift-independent measurements for all 59 galaxies (Table 12) below 3500 km s^{-1} in our survey.

4.4. Black Hole Mass, Bolometric Luminosity, and Eddington Ratios

We also provide the best BH mass measurements for each AGN in our catalog outside of continuum-dominated blazars (BZB). A small number of sources have direct (or higher-quality) measurements of BH masses, from reverberation mapping ($N = 48$), OH megamasers ($N = 10$), or high-quality IFU observations of gas or stars ($N = 12$), which we have adopted and tabulated when available.

Some AGNs may have multiple BH mass measurements from broad lines and velocity dispersions, so we select the best measurement (Table 13) based on the following ordered scheme:

Table 11
Newly Identified Redshifts

BAT Index	Swift Name	Counterpart	DR2 Type	Telescope	z	Line	A_V
25	SWIFT J0041.0+2444	SWIFT J004039.9+244539	Sy1.9	Palomar/DBSP	0.078365	[O III] λ5007	0.1
42	SWIFT J0057.0+6405	NVSS J005712+635942	BZQ	Palomar/DBSP	0.289627	[O III]	4.5
65	SWIFT J0116.5−1235	2MASX J01163118−1236171	Sy1.9	VLT/X-shooter	0.142447	[O III]	0.1
92	SWIFT J0149.2+2153A	LEDA 1656658	Sy1.9	Palomar/DBSP	0.069397	[O III]	0.3
154	SWIFT J0252.1−6758	2MASX J02513173−6803059	Sy1.9	VLT/X-shooter	0.18263	[O III]	0.1
161	SWIFT J0259.9+4419	2MASX J02593756+4417180	Sy1	Palomar/DBSP	0.031291	[O III]	0.7
210	SWIFT J0413.3+1659	MG1 J041325+1659	BZQ	Palomar/DBSP	0.211541	[O III]	2.1
240	SWIFT J0449.6−5515	2MASX J04500193−5512404	Sy2	VLT/X-shooter	0.021576	[O III]	0
250	SWIFT J0459.7+3502	LEDA 168924	Sy2	Palomar/DBSP	0.044383	[O III]	2.8
257	SWIFT J0505.6−6735	2MASX J05052442−6734358	Sy2	VLT/X-shooter	0.046517	[O III]	0.8
323	SWIFT J0612.2−4645	PMN J0612−4647	BZQ	VLT/X-shooter	0.317767	[O III]	0.2
333	SWIFT J0626.6+0729	LEDA 136513	Sy1	du Pont/BC	0.042447	[O III]	2
343	SWIFT J0640.0−4737	SWIFT J064013.50−474132.9	Sy2	VLT/X-shooter	0.057242	[O III]	0.4
353	SWIFT J0659.3+2406	2MASX J06591070+2401400	Sy2	Keck/LRIS	0.090822	[O III]	0.2
359	SWIFT J0709.3−1527	PKS 0706−15	BZB	Palomar/DBSP	0.142277	Gal. Temp.	2
367	SWIFT J0723.8−0804	1RXS J072352.4−080623	Sy1	Palomar/DBSP	0.144926	[O III]	0.9
380	SWIFT J0741.4−5447	2MASX J07410919−5447461	Sy2	VLT/X-shooter	0.106098	[O III]	0.5
396	SWIFT J0755.4+8402	2MASS J07581638+8356362	Sy1	Palomar/DBSP	0.133952	[O III]	0.15
433	SWIFT J0854.3−0827	SWIFT J085429.35−082428.6	Sy2	VLT/X-shooter	0.188435	[O III]	0.1
487	SWIFT J1007.4+6534	1RXSJ100712.6+653511	Sy1	Palomar/DBSP	0.126589	[O III]	0.2
494	SWIFT J1020.5−0237A	SDSS J102103.08−023642.6	Sy2	VLT/X-shooter	0.293645	[O III]	0.13
510	SWIFT J1041.4−1740	2MASX J10410120−1734300	Sy2	VLT/X-shooter	0.080844	[O III]	0.2
660	SWIFT J1310.9−5553	IGR J13109−5552	BZQ	VLT/X-shooter	1.55906	Mg II λ2798	1.1
745	SWIFT J1449.5+8602	2MASX J14545815+8554589	Sy2	Palomar/DBSP	0.111951	[O III]	0.5
747	SWIFT J1451.0−5540B	LEDA 3085605	Sy2	VLT/X-shooter	0.018663	Hα	2.5
756	SWIFT J1508.6−4953	PMN J1508−4953	BZQ	VLT/X-shooter	1.520201	Mg II λ2798	1.2
761	SWIFT J1512.2−1053A	NVSS J151148−105023	BZQ	Palomar/DBSP	0.94672	[O III]	0.34
762	SWIFT J1512.2−1053B	2MASX J15120505−1046356	Sy2	VLT/X-shooter	0.165799	[O III]	0.3
780	SWIFT J1548.1−6406	SWIFT J1548.1−6406	BZQ	VLT/X-shooter	1.693124	[O III]	0.6
792	SWIFT J1605.9−7250	LEDA 259433	Sy2	VLT/X-shooter	0.069271	[O III]	0.3
894	SWIFT J1733.3+3635	2MASX J17333689+3631319	Sy1.9	Palomar/DBSP	0.043661	[O III]	0.1
897	SWIFT J1737.7−5956A	1RXS J173751.2−600408	BZQ	VLT/X-shooter	3.656025	[O III]	0.2
906	SWIFT J1742.1−6054	PKS 1737−60	Sy1	SOAR/GM	0.152012	[O III]	0.2
974	SWIFT J1825.7+7215	LEDA 61865	Sy2	Palomar/DBSP	0.110806	[O III]	0.2
1000	SWIFT J1852.2+8424A	SWIFT J185024.2+842240	Sy1	Palomar/DBSP	0.183122	[O III]	0.3
1001	SWIFT J1852.2+8424B	1RXS J184642.2+842506	Sy1	Palomar/DBSP	0.225381	[O III]	0.3
1007	SWIFT J1852.8+3002	GALEXASC J185249.68+300425.8	Sy1.9	Palomar/DBSP	0.057301	[O III]	0.6
1066	SWIFT J2010.6−2521	1RXS J201020.0−252356	BZQ	VLT/X-shooter	0.824924	[O III]	0.5
1075	SWIFT J2024.0−0246	1RXS J202400.8−024527	Sy1.9	VLT/X-shooter	0.137523	[O III]	0.2
1078	SWIFT J2029.4−6149	2MASX J20293125−6149087	Sy2	VLT/X-shooter	0.124274	[O III]	0.2
1083	SWIFT J2034.0−0943	2MASX J20341926−0945586	Sy2	VLT/X-shooter	0.081551	[O III]	0.2
1091	SWIFT J2048.4+3815	1RXS J204826.8+381120	Sy1	Palomar/DBSP	0.105394	[O III]	2.8
1096	SWIFT J2059.6+4301B	SWIFT J210001.06+430209.6	Sy2	Palomar/DBSP	0.066023	[O III]	4.1
1105	SWIFT J2117.5+5139	2MASX J21174741+5138523	BZQ	Palomar/DBSP	0.053392	[S II] λ9531	9.7
1130	SWIFT J2156.2+1724	2MASX J21561518+1722525	Sy1.8	VLT/X-shooter	0.03417	[O III]	0.3
1164	SWIFT J2243.2−4539	2MASX J22422135−4539093	Sy1.9	VLT/X-shooter	0.120675	[O III]	0
1208	SWIFT J2352.6−1707	2MASX J23525143−1704370	Sy1	du Pont/BC	0.054695	[O III]	0.1

Note. Column descriptions are the same as in Table 1, unless otherwise noted. A detailed description of this table's contents is given in Section 4.

1. Literature measurements with megamasers, reverberation mapping, or stellar and gas dynamics.
2. Broad-line Hβ if $N_{\rm H} < 10^{22}$ cm^{-2} from Mejía-Restrepo et al. (2022). The conversion of broad-line measurements to BH masses is given by Trakhtenbrot & Netzer (2012).
3. Broad-line Hα from Mejía-Restrepo et al. (2022) if $N_{\rm H} < 10^{22}$ cm^{-2} and broad-line Hβ is present but not measurable because of instrumental or telluric issues. They use Greene & Ho (2005), but adjusted by 4/3 (or +0.125 dex) for a consistent virial factor of 1 across all broad-line measurements.
4. Broad-line Mg II λ2798 followed by C IV λ1549 for high-redshift sources ($z > 0.8$) from Mejía-Restrepo et al. (2022) for those without broad-line Hβ using the relation of Mejia-Restrepo et al. (2016).
5. Stellar velocity dispersion measurements for all Sy1.9 and Sy2 AGNs from Koss et al. (2022b). We calculated

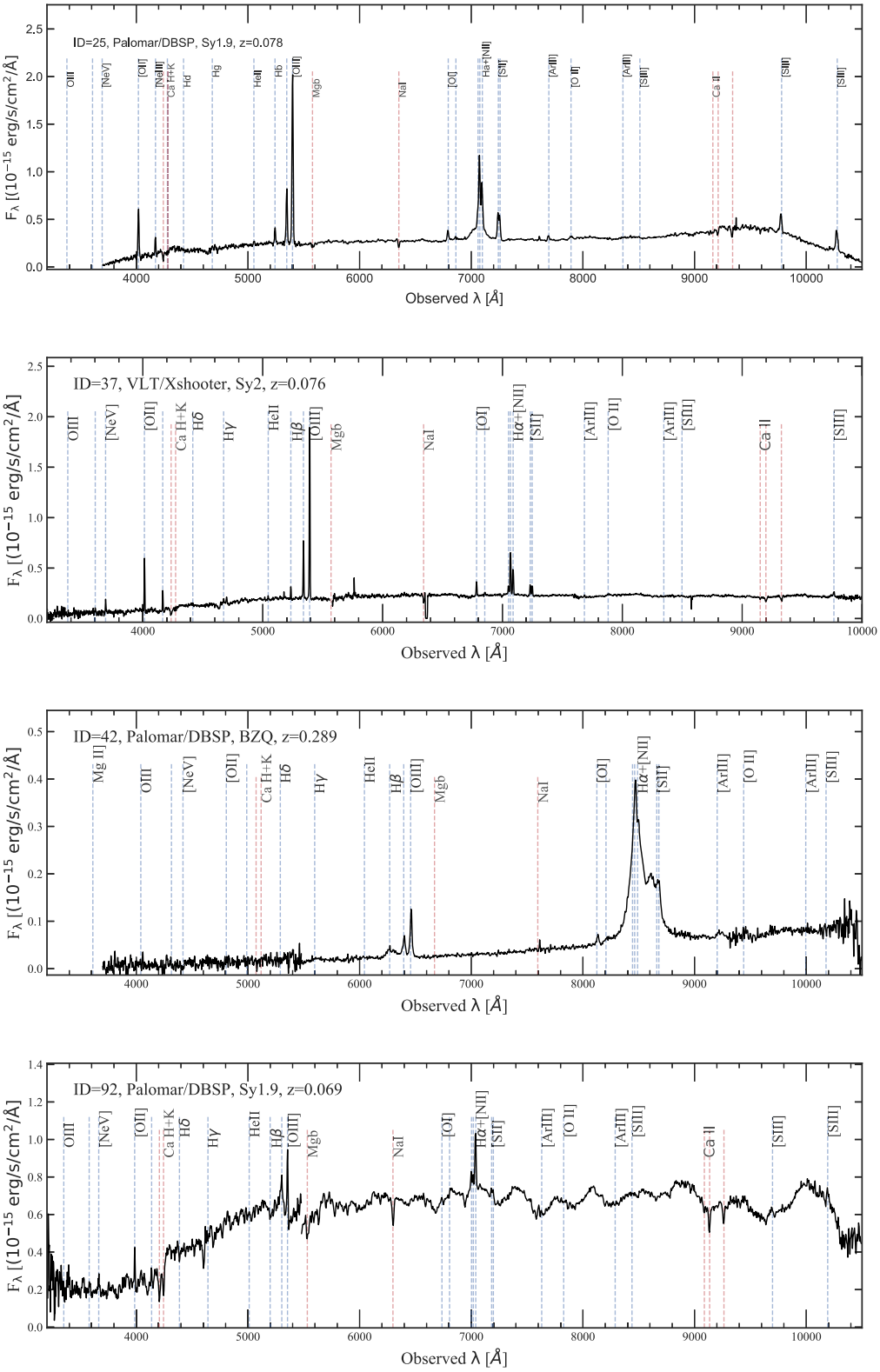

Figure 7. Examples of 47 sources with newly identified redshifts.

the BH mass, $M_{\rm BH}$, using the $M_{\rm BH}$–σ_* relation of Equation (13) from Kormendy & Ho (2013).

6. If $N_{\rm H} > 10^{22}$ cm^{-2}, and if no velocity dispersion measurement is possible, broad-line Hα followed by broad-line Hβ is used from Mejía-Restrepo et al. (2022). These final measurements should be used with caution because of the tendency to underestimate $M_{\rm BH}$ due to obscuration (e.g., Ricci et al. 2022; den Brok et al. 2022; Mejía-Restrepo et al. 2022).

A summary of the number of best BH mass measurements is found in Figure 8. The majority of measurements come from

Table 12
Redshift-independent Distances

BAT ID	Counterpart	z	Dist. Ind. (Mpc)[a]	Dist. z (Mpc)	Method[b]
655	NGC 4945	0.002259	3.72	9.7	TRGB
671	CenA	0.001877	3.66	8.1	TRGB
477	M81	−0.000113	3.61	0	TRGB
711	Circinus galaxy	0.001495	4.21	6.4	NED
616	NGC 4395	0.001106	4.76	4.7	TRGB
609	NGC 4258	0.001692	7.31	7.3	TRGB
585	NGC 4051	0.002043	11.02	8.8	CF3
838	NGC 6221	0.004108	11.86	17.6	CF3
731	NGC 5643	0.004042	12.68	17.4	TRGB
875	NGC 6300	0.003131	13.18	13.4	CF3
593	NGC 4138	0.003187	13.7	13.7	SBF
144	NGC 1068	0.003484	14.4	15	NED
579	NGC 3998	0.003574	14.19	15.3	SBF
686	NGC 5273	0.003606	16.6	15.5	SBF
1157	NGC 7314	0.004607	16.75	19.8	CF3
548	NGC 3718	0.003278	17.1	14.1	NED
216	NGC 1566	0.00474	17.9	20.4	TRGB
615	NGC 4388	0.008344	18.11	36	CF3
595	NGC 4151	0.003152	19	13.5	NED
665	NGC 5033	0.002763	19.05	11.9	CF3
140	NGC 1052	0.004519	19.23	19.4	SBF
590	NGC 4102	0.002365	19.5	10.1	CF3
184	NGC 1365	0.005091	19.57	21.9	TRGB
653	NGC 4941	0.003881	20.45	16.7	NED
484	NGC 3079	0.003505	20.61	15	CF3
1142	NGC 7213	0.004767	22	20.5	NED
1188	NGC 7582	0.005249	22.49	22.6	CF3
1046	NGC 6814	0.005792	22.8	24.9	NED
497	NGC 3227	0.003277	22.95	14.1	NED
436	NGC 2655	0.004854	24.4	20.9	NED
712	NGC 5506	0.005979	26.4	25.7	NED
607	NGC 4235	0.007934	26.6	34.2	SBF
1180	NGC 7465	0.006343	27.2	27.3	NED
319	ESO 5-4	0.006162	28.18	26.5	CF3
437	NGC 2712	0.006754	31.19	29.1	CF3
480	NGC 3081	0.008071	32.5	34.8	NED
1135	NGC 7172	0.008511	33.9	36.7	NED
823	ESO 137-34	0.008759	34.1	37.8	NED
308	NGC 2110	0.0075	34.3	32.3	NED
93	NGC 678	0.009485	34.5	40.9	NED
688	NGC 5290	0.008566	34.51	36.9	CF3
621	NGC 4500	0.010357	34.51	44.7	CF3
1184	NGC 7479	0.007105	36.81	30.6	CF3
631	NGC 4593	0.00832	37.2	35.9	NED
739	NGC 5728	0.010321	37.5	44.6	CF3
471	NGC 2992	0.007675	38	33.1	NED
558	NGC 3783	0.008958	38.5	38.6	NED
103	LEDA 89913	0.011836	38.8	51.2	NED
530	NGC 3516	0.008718	38.9	37.6	NED
654	NGC 4939	0.010543	42.07	45.5	CF3
599	NGC 4180	0.006532	43.05	28.1	CF3
560	NGC 3786	0.008916	43.9	38.4	NED
766	NGC 5899	0.008597	45.08	37.1	CF3
1092	IC 5063	0.011267	45.9	48.7	NED
237	LEDA 86269	0.010529	46.13	45.5	CF3
62	IC 1657	0.011688	48.31	50.5	CF3
58	NGC 424	0.010885	51.05	47	CF3
684	NGC 5283	0.010365	51.52	44.7	CF3
451	IC 2461	0.007535	58.88	32.5	CF3

Notes.
[a] Best redshift-independent distance. See Section 4.2 for a detailed description of the redshift-independent measurements.
[b] TRGB: tip of the red giant branch (e.g., McQuinn et al. 2017); CF3: Cosmicflows-3 project (Courtois et al. 2017); NED: NASA Extragalactic Database.

Table 13
Summary of Best Black Hole Mass Method

Best Black Hole Mass Method	Count
$\sigma_\star$	344
Hβ	305
Lit.	62
Hα ($N_{\rm H} > 10^{22}$ cm^{-2})	37
Hα	13
Mg II λ2798	11
C IV λ1549	10
C IV λ1549 ($N_{\rm H} > 10^{22}$ cm^{-2})	4
Mg II λ2798 ($N_{\rm H} > 10^{22}$ cm^{-2})	3
Hβ ($N_{\rm H} > 10^{22}$ cm^{-2})	1
Total	790

Note. The best BH mass measurement provided in the catalog. See Section 4.2 for details.

either velocity dispersion measurements or broad Hβ, with a smaller number from literature measurements, broad Hα, broad Hα in X-ray-obscured AGNs ($N_{\rm H} > 10^{22}$ cm^{-2}), and Mg II λ2798 or C IV λ1549 broad lines for distant beamed AGNs ($z > 1$). See Mejía-Restrepo et al. (2022) and Koss et al. (2022b) for more details about the individual observations, calculations, and methodologies.

The bolometric luminosity is calculated from the intrinsic luminosity in the 14–150 keV range as shown in Ricci et al. (2017a; see their Table 12). This analysis was done using the 0.3–150 keV range by combining the 70-month average Swift BAT spectra with data below 10 keV from Swift XRT, XMM-Newton, Chandra, Suzaku, and ASCA using detailed spectral models. Here we calculated the bolometric luminosity using a 14–150 keV bolometric correction of 8 based on the factor of 20 for the 2–10 keV range (Vasudevan & Fabian 2009) and assuming $\Gamma = 1.8$. We prefer this rather than using the direct calculation from the 2–10 keV range because the corrections are less dependent on $N_{\rm H}$ for Compton-thick AGNs. The 14–150 keV emission is also integrated over 70 months, so it is more likely to be representative of the average value.

For Eddington ratios we assume an Eddington luminosity consistent with solar metallicity:

$$L_{\rm Edd} = 1.5 \times 10^{46}\ {\rm erg\ s^{-1}} \frac{M_{\rm BH}}{10^8 M_\odot}. \quad (1)$$

We note that more complicated procedures than simple bolometric corrections from the intrinsic X-ray flux such as in terms of the Eddington ratio ($L/L_{\rm Edd}$) are sometimes used (e.g., Marconi et al. 2004; Lusso et al. 2011). However, we prefer this simple approach, similar to what was done in the BASS DR1, that can be reliably applied to all AGNs.

We do not list individual errors for each $M_{\rm BH}$, $L_{\rm bol}$, and $L/L_{\rm Edd}$ measurement, as they are dominated by the systematic uncertainties in the scaling relations rather than the emission-line fitting or velocity dispersion measurements, which are typically <0.1 dex. Errors in $M_{\rm BH}$ are of order 0.4–0.5 dex owing to systematic uncertainties in virial and σ_*-based scaling relations (e.g., McLure & Dunlop 2002; Vestergaard & Peterson 2006; Ricci et al. 2022). For $L_{\rm bol}$, the scatter between BAT 14–195 keV luminosity and L_{5100} was 0.46 dex in the DR1 (Koss et al. 2017)

Efforts are currently underway for future BASS surveys to better calibrate the bolometric correction with AGN source properties and estimate its intrinsic reliability. A large (>100 AGN) HST program is currently underway obtaining high spatial resolution near-UV (<3000 Å) imaging of the AGN

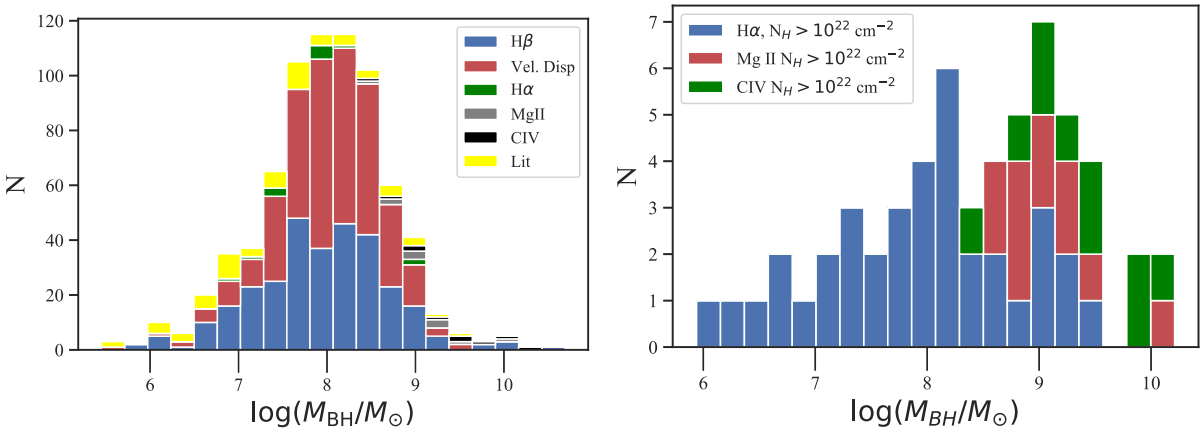

Figure 8. Left: histogram of the BH mass estimates excluding broad-line measurements in X-ray-obscured AGNs ($N_{\rm H} > 10^{22}$ cm^{-2}). Right: histogram of the BH mass estimates in the small number of X-ray-obscured AGNs with only broad-line measurements. While many of these AGNs do have BH masses consistent with the other unobscured distribution (e.g., $>10^7\ M_\odot$), there is a larger fraction with low masses ($<10^7\ M_\odot$) that may be significantly underestimated.

Table 14
Summary of Unbeamed AGN Properties

Type	N	N $\lvert b\rvert > 10°$	z	$N_{M_{\rm BH}}$	$N_{M_{\rm BH}}$ $\lvert b\rvert > 10°$	% Meas. $M_{\rm BH}$	% Meas. $\lvert b\rvert > 10°$	log $M_{\rm BH}$ ($M_\odot$)	log $L_{\rm bol}$ (erg s^{-1})	log $L/L_{\rm Edd}$	log $N_{\rm H}$ (cm^{-2})
(1)	(2)	(3)	(4)	(5)	(6)	(7)	(8)	(9)	(10)	(11)	(12)
Sy1	359	318	0.050 ± 0.003	350	311	97	98	7.81 ± 0.04	44.87 ± 0.04	-1.17 ± 0.03	20.0 ± 0.05
Sy1.9	101	86	0.030 ± 0.004	97	84	96	98	7.98 ± 0.06	44.59 ± 0.08	-1.61 ± 0.09	22.28 ± 0.13
Sy2	292	259	0.029 ± 0.003	275	253	94	98	8.06 ± 0.04	44.50 ± 0.04	-1.71 ± 0.04	23.27 ± 0.05
Total	752	663	0.038±0.002	722	648	96	98	7.96 ± 0.03	44.67 ± 0.03	-1.42 ± 0.03	21.98 ± 0.06

Note. Summary of the medians and standard error of the median for different populations of unbeamed AGN. Column (1): AGN optical type based on the presence of broad Hβ and Hα. Column (2): total for the whole sample. Column (3): total excluding the Galactic plane region $|b| < 10°$, where high optical extinction makes measurements more difficult. Column (4): median redshift from optical lines. Columns (5)–(8): number of unique AGNs with $M_{\rm BH}$ measurements and excluding the Galactic plane region $|b| < 10°$, where high optical extinction makes measurements more difficult. Also listed as percentages. Columns (9)–(12): median $M_{\rm BH}$, $L_{\rm bol}$, $L/L_{\rm Edd}$, and $\log(N_{\rm H}/{\rm cm}^{-2})$ for the sample.

Table 15
Summary of Beamed AGN Properties

Type	N	N, $\lvert b\rvert > 10°$	z	$N_{M_{\rm BH}}$	% Meas. $M_{\rm BH}$	log $M_{\rm BH}$	log $L_{\rm bol}$	log $L/L_{\rm Edd}$	log $N_{\rm H}$
(1)	(2)	(3)	(4)	(5)	(6)	(7)	(8)	(9)	(10)
BZQ	74	63	0.88 ± 0.12	67	91	8.83 ± 0.09	47.66 ± 0.16	0.38 ± 0.12	20 ± 0.11
BZB	22	18	0.13 ± 0.02				45.81 ± 0.12		20.57 ± 0.12
BZG	8	6	0.07 ± 0.02				45.11 ± 0.20		20.81 ± 0.11
Sy1/Lense	1	1	0.65	1	100	8.79	47.18	0.21	20
BZQ/Lense	1	0	2.51				49.49		22.77
Total	106	88	0.33 ± 0.10	68		8.83 ± 0.09	46.53 ± 0.14	0.38 ± 0.12	20.54 ± 0.08

Note. Summary of the medians and standard error of the median for different populations of beamed and/or lensed AGNs. Column (1): AGN optical type based on presence of broad lines (BZQ), only host galaxy features lacking broad lines (BZG), or traditional continuum-dominated blazars with no emission lines (BZB), or lensing. Column (2): total for the whole sample. Column (3): total excluding the Galactic plane region $|b| < 10°$, where high optical extinction makes measurements more difficult. Column (4): median redshift from optical lines. Columns (5)–(6): number of unique AGNs with $M_{\rm BH}$ measurements and percentages. Columns (7)–(10): median $M_{\rm BH}$, $L_{\rm bol}$, $L/L_{\rm Edd}$, and $\log(N_{\rm H}/{\rm cm}^{-2})$ for the sample.

emission, combined with simultaneous measurement of the AGN emission in the X-rays and UV/optical from Swift, with ground-based imaging in *griz*.

A summary of the survey completeness in BH mass measurements for unbeamed AGNs is provided in Table 14 separated by AGN type. Overall the completeness is slightly higher for Sy1 and Sy1.9 (>96%) than for velocity dispersion measurements (>93%). Outside of the Galactic plane ($|b| > 10°$) the survey completeness rises to 98% for all unbeamed AGNs because of the typically lower extinction in these regions. Finally, for beamed AGNs with broad lines (BZQ) the measured BH masses (Table 14) and completeness are somewhat lower, but still the majority (91%).

A summary of the typical BH masses, bolometric luminosities, Eddington ratios, and X-ray column densities is provided

in Tables 14 and 15 for unbeamed and beamed AGNs, respectively.

5. Summary

We have presented an overview of the BASS DR2 survey with 1449 optical spectra, of which 1182 are released for the first time, for the 858 hard-X-ray-selected AGNs in the Swift BAT 70-month sample. With this first DR2 catalog release we provide the following:

1. A revised catalog based on optical and NIR spectroscopic follow-up that identifies all 858 among unknown sources above ($|b| > 3°$) or below $A_V = 5$ mag, excluding only seven unknown sources deep within the Galactic plane at high extinction. We have included new identifications of 17 Galactic sources.
2. We have further classified our sources by AGN type based on the presence of broad lines (e.g., Sy1, Sy1.9, Sy2), as well as beamed and lensed AGNs. We have further provided important catalogs for population studies including dual AGNs, weakly associated AGNs, and multiple weak confused sources within the BAT beam.
3. A full master catalog summary of the 1449, instrumental settings, their reductions, and observing conditions. With this we have provided a master catalog of redshifts, distances, bolometric luminosities, and BH masses.
4. Overall the completion for the survey is 99.9% in redshift outside the extreme regions in the Galactic plane ($|b| > 3°$). In BH mass, the survey is 98% complete using broad lines and velocity dispersions for unbeamed AGNs outside the Galactic plane ($|b| > 10°$). The final catalog contains 47 new redshift measurements and 790 BH mass measurements.

We thank the reviewer for the constructive comments that helped us improve the quality of this paper.

BASS/DR2 was made possible through the coordinated efforts of a large team of astronomers, supported by various funding institutions, and using a variety of facilities.

We acknowledge support from NASA through ADAP award NNH16CT03C (M.K.); the Israel Science Foundation through grant No. 1849/19 (B.T.); the European Research Council (ERC) under the European Union's Horizon 2020 research and innovation program, through grant agreement No. 950533 (B. T.); FONDECYT Postdoctorado 3180506 (F.R.) and 3210157 (A.R.); FONDECYT Regular 1190818 (E.T., F.E.B.) and 1200495 (E.T., F.E.B.); ANID grants CATA-Basal AFB-170002, ACE210002, and FB210003 (C.R., F.R., E.T., F.E.B., and E.C.); ANID Anillo ACT172033 (E.T.); Millennium Science Initiative Program—ICN12_009 (F.E.B.); an ESO fellowship (M.H., J.M.); and Fondecyt Iniciacion grant 11190831 (C.R.). K. O. acknowledges support from the National Research Foundation of Korea (NRF-2020R1C1C1005462) and the Japan Society for the Promotion of Science (JSPS, ID: 17321); I.L. acknowledges support from the Comunidad de Madrid through the Atracción de Talento Investigador Grant 2018-T1/TIC-11035, C.M.U. acknowledges support from the National Science Foundation under grant No. AST-1715512, F.P. acknowledges support from a Clay Fellowship administered by the Smithsonian Astrophysical Observatory, and from the Black Hole Initiative at Harvard University, which is funded by grants from the John Templeton Foundation and the Gordon and Betty Moore Foundation, M.B. acknowledges support from the YCAA Prize Postdoctoral Fellowship; R.R. thanks CNPq (311223/2020-6), CAPES, and FAPERGS (16/2551-0000251-7 and 19/2551-0001750-2). This work was performed in part at Aspen Center for Physics, which is supported by National Science Foundation grant PHY-1607611.

We also acknowledge the following people who assisted in acquiring the Palomar observations presented herein: Dave Alexander, Roberto Assef, Rosamaria Carraro, Alison Dugas, Peter Eisenhardt, Clarke Esmerian, Carla Fuentes, Felix Fuerst, Maya Fuller, Daniel Gawerc, David Girou, Ana Glidden, Matthew Graham, Claire Greenwell, Brian Grefenstette, Marianne Heida, Hyunsung Jun, Peter Kosec, Stephanie LaMassa, Jeff Maggio, Alejandra Melo, Catalina-Ana Miritescu, Wenli Mo, Eric Mukherjee, Gael Noirot, Antonija Oklopčić Sean Pike, Joseph Simon, Tawny Sit, Navin Sridhar, Aaron Stemo, Becky Tang, Thomas Venville, Jingyi Wang, and Dominika Wylezalek. We acknowledge financial contributions from Joanna Wall Muir and the California Institute of Technology's Student Faculty Program to assist in the Palomar observations for Tea Freedman-Susskind, Feiyang Liu, Milan Robertson, Yerong Xu, and Emily Zhang. We acknowledge the work that the Swift BAT team has done to make this project possible.

We acknowledge the various telescopes used in this paper. We are tremendously thankful to all the observing and support staff in all the observatories, and their headquarters, for their great assistance in planning and conducting the observations that made BASS/DR2 possible. Specifically, BASS/DR2 is based on the following:

(1) Observations collected at the European Organisation for Astronomical Research in the Southern Hemisphere under 34 ESO programs: 60.A-9024(A), 60.A-9421(A), 062.H-0612(A), 086.B-0135(A), 089.B-0951(A), 089.B-0951(B), 090.A-0830(A), 090.D-0828(A), 091.B-0900(B), 091.C-0934(B), 092.B-0083(A), 093.A-0766(A), 094.B-0321(A), 095.B-0059(A), 098.A-0062, 098.A-0635(B), 098.B-0551(A), 099.A-0403(A+B), 099.A-0442(A), 099.B-0785(A), 0101.A-0765(A), 0101.B-0456(B), 0101.B-0739(A), 0102.A-0433(A), 0102.B-0048, 0103.A-0521(A), 0103.B-0566(A), 0103.A-0777(A), 0104.A-0353(A), 0104.B-0959(A), 0106.A-0521(A), 385.B-1035(A), 2100.B-5018(B), and 60.A-9100(J).

(2) Data obtained with the Hale 200-inch telescope at Palomar observatory, including five dedicated Yale programs: 2017B/Y04, 2018A/Y03, 2018B/Y04, 2019A/Y03, and 2019B/Y04 (PI: M. Powell). Additional data were obtained as part of Caltech runs including 2014B/P05, 2015A/P04, 2015B/P06, 2016A/P06, 2016B/P04, 2017A/P13, 2017B/P01, 2018A/P15, 2018B/P02, 2019A/P18, 2019B/P11, 2020A/P14, and 2020B/P19 (PI: F. Harrison) and also JPL runs including 2016B/J12, 2017A/J07, 2017B/J15 2019B/J09, 2019A/J06, 2019B/J19, 2020A/J11, and 2020B/J04 (PI: D. Stern).

(3) Observations obtained at the Southern Astrophysical Research (SOAR) telescope, which is a joint project of the Ministério da Ciência, Tecnologia e Inovações (MCTI/LNA) do Brasil, the US National Science Foundation's NOIRLab, the University of North Carolina at Chapel Hill (UNC), and Michigan State University (MSU). These include from CNTAC (CN2018A-104, CN2018B-83) and NOIRLab program 2012A-0463 (PI M. Trippe).

(4) Observations at Kitt Peak National Observatory at NSF's NOIRLab (NOIRLab Prop. ID 52, 2946; PI: F. Bauer), which is managed by the Association of Universities for Research in Astronomy (AURA) under a cooperative agreement with the

National Science Foundation. We are honored to be permitted to conduct astronomical research on Iolkam Du'ag (Kitt Peak), a mountain with particular significance to the Tohono O'odham.

(5) Data gathered with the 6.5 m Magellan Telescopes (CN2019A-70 and CN2019B-77) and the 2.5 m du Pont telescope (CN2016A-80) located at Las Campanas Observatory, Chile. Support for the design and construction of the Magellan Echellette Spectrograph was received from the Observatories of the Carnegie Institution of Washington, the School of Science of the Massachusetts Institute of Technology, and the National Science Foundation in the form of a collaborative Major Research Instrument grant to Carnegie and MIT (AST0215989).

(6) Data obtained at the W. M. Keck Observatory, which is operated as a scientific partnership among the California Institute of Technology, the University of California, and the National Aeronautics and Space Administration. The Observatory was made possible by the generous financial support of the W. M. Keck Foundation. The authors wish to recognize and acknowledge the very significant cultural role and reverence that the summit of Maunakea has always had within the indigenous Hawaiian community. We are most fortunate to have the opportunity to conduct observations from this mountain.

(7) Data obtained as part of the various stages of the Sloan Digital Sky Survey (SDSS-I/II, III, and IV). Funding for the SDSS has been provided by the Alfred P. Sloan Foundation, the US Department of Energy Office of Science, and the Participating Institutions. SDSS acknowledges support and resources from the Center for High Performance Computing at the University of Utah. The SDSS website is www.sdss.org. The most recent generation of the SDSS we benefited from, SDSS-IV, is managed by the Astrophysical Research Consortium for the Participating Institutions of the SDSS Collaboration, including the Brazilian Participation Group, the Carnegie Institution for Science, Carnegie Mellon University, Center for Astrophysics | Harvard & Smithsonian, the Chilean Participation Group, the French Participation Group, Instituto de Astrofísica de Canarias, Johns Hopkins University, Kavli Institute for the Physics and Mathematics of the Universe (IPMU)/University of Tokyo, the Korean Participation Group, Lawrence Berkeley National Laboratory, Leibniz Institut für Astrophysik Potsdam (AIP), Max-Planck-Institut für Astronomie (MPIA Heidelberg), Max-Planck-Institut für Astrophysik (MPA Garching), Max-Planck-Institut für Extraterrestrische Physik (MPE), National Astronomical Observatories of China, New Mexico State University, New York University, University of Notre Dame, Observatário Nacional/MCTI, The Ohio State University, Pennsylvania State University, Shanghai Astronomical Observatory, United Kingdom Participation Group, Universidad Nacional Autónoma de México, University of Arizona, University of Colorado Boulder, University of Oxford, University of Portsmouth, University of Utah, University of Virginia, University of Washington, University of Wisconsin, Vanderbilt University, and Yale University.

This research has made use of the NASA/IPAC Extragalactic Database (NED), which is operated by the Jet Propulsion Laboratory, California Institute of Technology, under contract with the National Aeronautics and Space Administration. This research has made use of the SIMBAD database, operated at CDS, Strasbourg, France.

A significant part of the BASS observations and work took place during the COVID-19 crisis. We thank the healthcare experts in communities around the world, for their tireless efforts to keep us all as safe and healthy as possible.

Facilities: Du Pont (Boller & Chivens spectrograph), Keck:I (LRIS), Magellan:Clay, Hale (Doublespec), NuSTAR, Swift (XRT and BAT), VLT:Kueyen (X-shooter), VLT:Antu (FORS2), SOAR (Goodman).

Software: Astropy (Collaboration et al. 2013), ESO Reflex (Freudling et al. 2013), IRAF (National Optical Astronomy Observatories 1999), Matplotlib (Hunter 2007), `molecfit` (Smette et al. 2015), Numpy (van der Walt et al. 2011), Pandas (https://doi.org/10.5281/zenodo.3630805), `PySpecKit` (Ginsburg & Mirocha 2011).

Appendix A
Comparison to DR1 and Past Surveys

Here we provide a comparison to the 641 optical spectroscopic measurements from the BASS DR1 including redshifts, AGN classification, and BH mass measurements, as well as past measurements in the literature.

A.1. Beamed AGN Changes in DR2

Here we provide a list of all beamed AGNs that are newly identified or changed in DR2 in Table 16 compared to the DR1. Example spectra for the various classes (e.g., BZB, BZG, BZQ) are found in Figure 9.

A.2. AGN Classification

Overall, there are 168 DR2 AGNs that we provided revised or the first classification of AGN type based on our measurements. For comparison, we first look at the 641 DR1 AGN types compared to overlapping DR2 AGN types. There are 10% changes (64/641). This includes 52 reclassifications from Sy2 to Sy1.9 or Sy1, or from Sy1.9 to Sy1 based on the detection of broad lines that were not detected in DR1 spectra. Conversely, 12 spectra change from Sy1 to Sy1.9 or Sy2 or from Sy1.9 to Sy2. This shift largely reflects the higher-quality spectra in terms of resolution and signal-to-noise ratio compared to the archival DR1, which used much smaller telescopes and lower spectral resolutions rather than "bona fide" AGNs that have undergone changes. The "bona fide" changing optical type AGNs are part of a future study (M. Temple et al. 2022, in preparation). Among the 216 AGNs that were not part of the DR1 release, roughly half have their first or revised classifications (48%; 103/216). This is compared to the most recent 105-month survey (Oh et al. 2018), which includes updates from SIMBAD and NED. From these 103, 72 measurements are to previously unknown AGNs without available optical spectroscopy or classification.

A.3. Redshifts

We compare the redshifts from the 599 DR1 to the revised measurements from spectroscopy in DR2. Among the low-redshift sample ($z < 0.3$), the agreement is excellent, with no differences larger than 1000 km s^{-1}. At higher redshift ($0.3 > z > 1$) the median offset increases ($|z_{\rm DR2} - z_{\rm DR1}| = 157$ km s^{-1}), and finally increases to 1180 km s^{-1} at $z > 1$ owing to the use of the intrinsically broad lines of Mg II λ2798 and C IV λ1549 for the derivation of the redshift.

Table 16
Beamed AGN Changes in DR2

BAT ID	Swift Name	DR1 Class[a]	DR2 Type	References
30	SWIFT J0042.9+3016B		BZQ	P19
33	SWIFT J0048.8+3155	BZB	Sy2	P19
59	SWIFT J0113.8+2515		BZQ	P19
140	SWIFT J0241.3−0816	BZU	Sy2	P19
170	SWIFT J0312.9+4121	BZU	Sy1	T78
173	SWIFT J0319.7+4132	BZU	Sy2	P19
178	SWIFT J0326.0−5633		BZG	P19
226	SWIFT J0433.0+0521	BZU	Sy1	P19
273	SWIFT J0519.5−3140	BZU	Sy1	A19
277	SWIFT J0525.3−4600	BZQ	Sy2	P19
323	SWIFT J0225.0+1847		BZQ	P19
359	SWIFT J1959.6+6507		BZB	P19
377	SWIFT J0733.9+5156		BZG	P19
660	SWIFT J1310.9−5553		BZQ	P19
671	SWIFT J1325.4−4301	BZU	Sy2	P19
690	SWIFT J1347.1+7325		BZQ	P19
761	SWIFT J1943.5+2120		BZQ	P19
780	SWIFT J1145.6−6956		BZQ	P19
787	SWIFT J1557.8−7913	BZU	Sy2	P19
876	SWIFT J1719.7+4900	BZU	Sy1.9	P19
897	SWIFT J1458.9+7143		BZQ	P19
906	SWIFT J1742.1−6054	BZU	Sy1	B16
1082	SWIFT J2033.4+2147		BZQ	P19
1105	SWIFT J2117.5+5139		BZQ	P19
1142	SWIFT J2209.4−4711	BZU	Sy1.9	P19
1181	SWIFT J2303.1−1837	BZU	Sy1	P19

Notes. Column descriptions are the same as in Table 1, unless otherwise noted.
[a] Beamed AGN type in BASS DR1 (Koss et al. 2017).
References. A19: Angioni et al. (2019); B16: Bassani et al. (2016); P19: Paliya et al. (2019); T78: Tzanetakis et al. (1978).

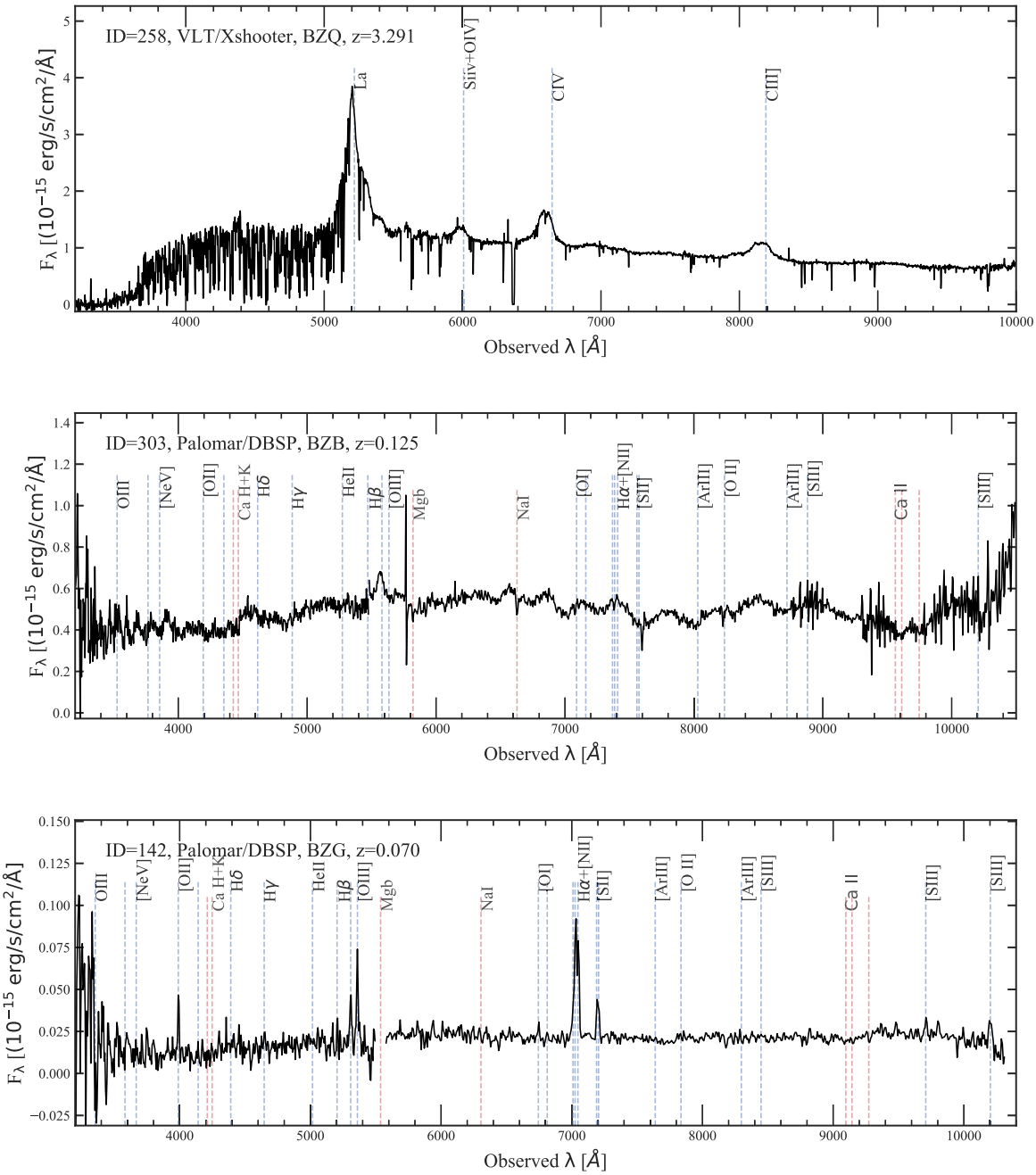

Figure 9. Figure showing the spectral classification of beamed sources based on the presence of broad lines (BZQ, top), traditional continuum-dominated blazars with no emission lines or host galaxy features (BZB, middle), or only host galaxy features lacking broad lines (BZG, bottom).

Appendix B
Example Spectra

Here we provide example spectra of various classes of AGNs and telescope setups not shown earlier in the text (Figures 10 and 11). Example spectra for each AGN will also be provided at the BASS website.[39]

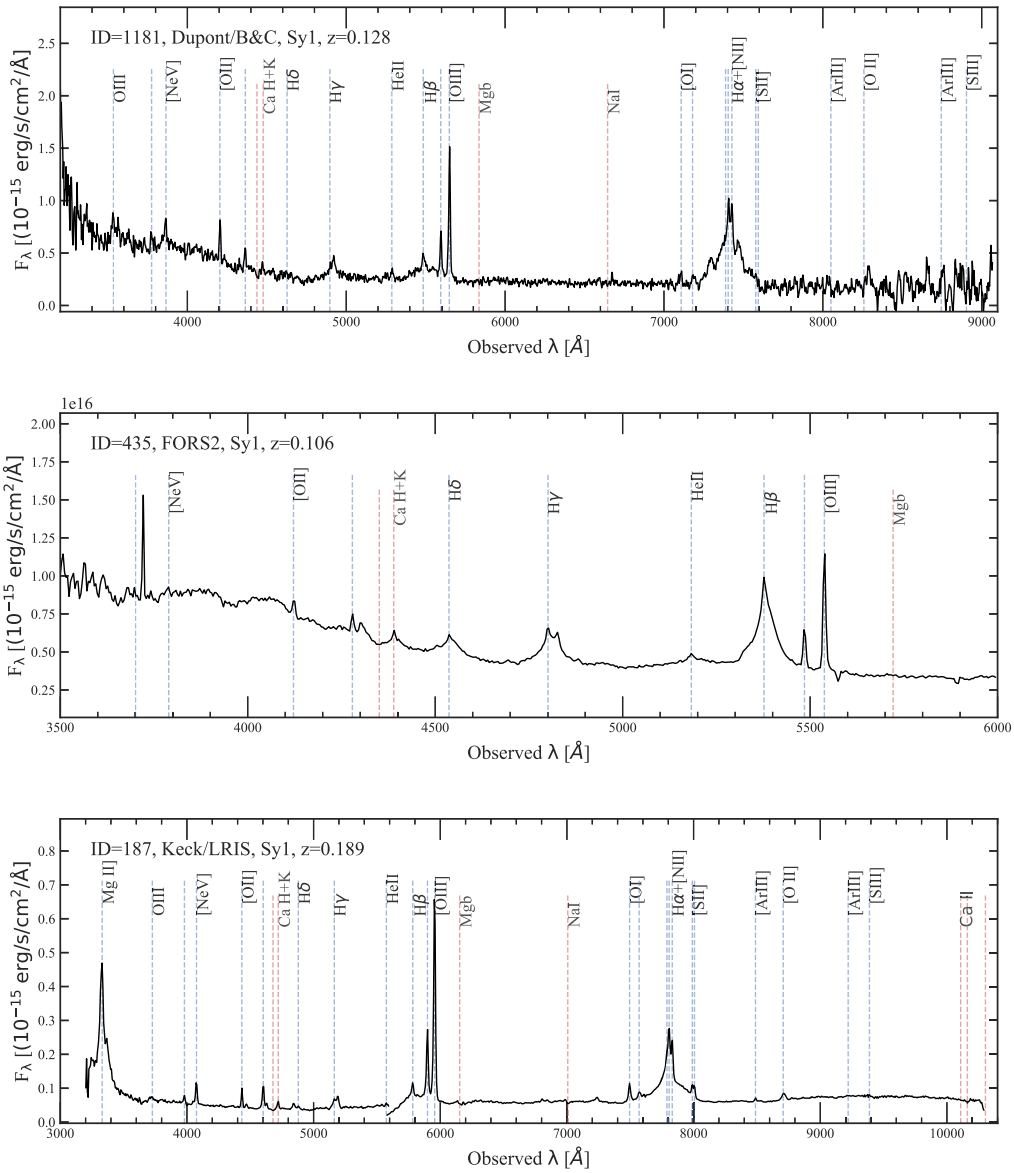

Figure 10. Figure showing examples of spectral setups not shown earlier in the text excluding the archival observations. A spectrum from the du Pont telescope with the Bollens & Chivens spectrograph with the 300 line mm^{-1} grating is shown in the top panel, a spectrum from the VLT with the FORS2 instrument is shown in the middle panel, and a spectrum with Keck using the LRIS instrument is shown in the bottom panel.

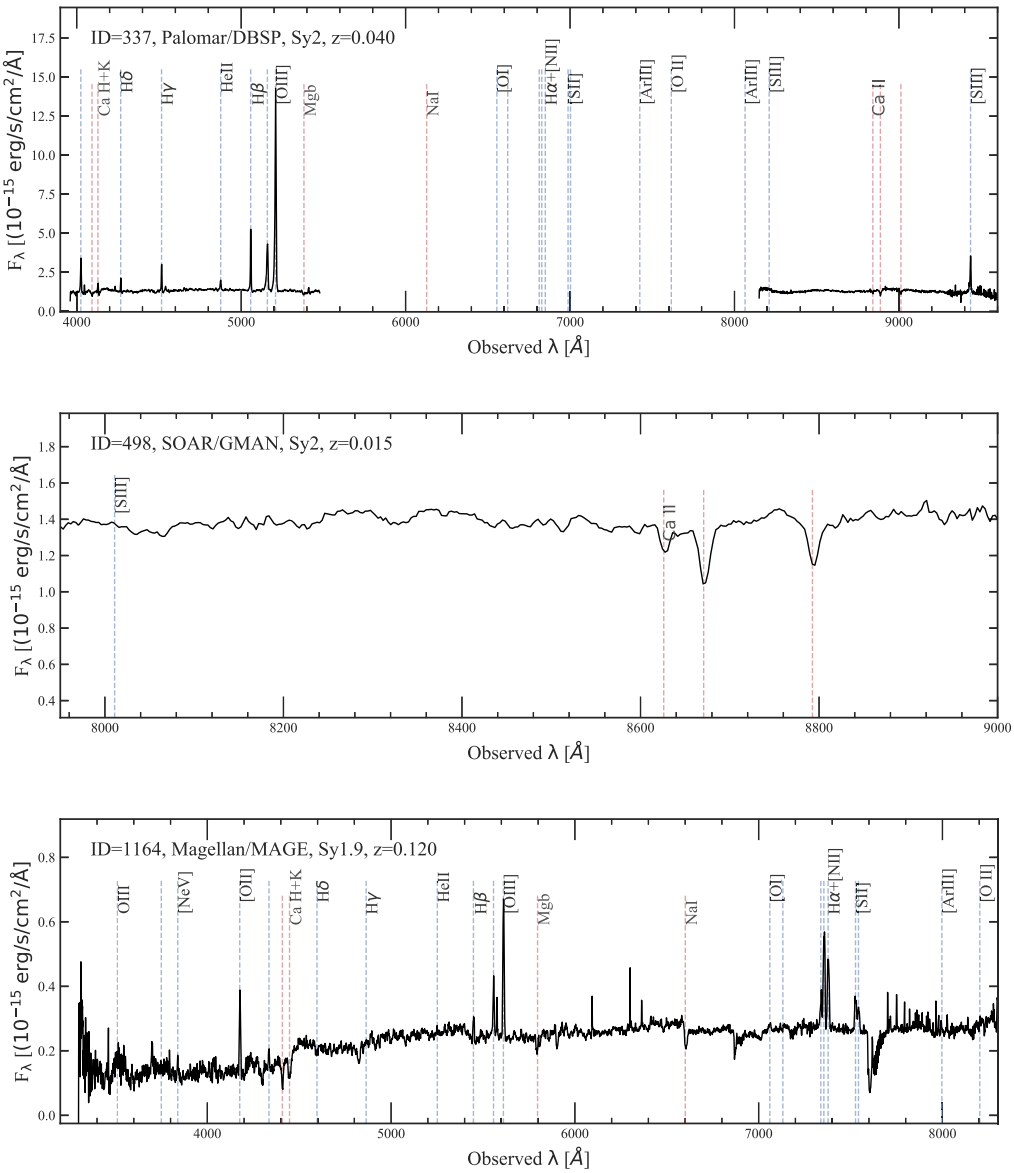

Figure 11. Figure showing examples of high-resolution spectral setups not shown earlier in the text excluding the archival observations. Spectra taken at the Palomar telescope with the Doublespec instrument with the 1200 line mm^{-1} grating are shown in the top panel, with spectra from SOAR with 1200 line mm^{-1} grating using the Goodman instrument shown in the middle panel and finally an echelle spectrum from Magellan using the magE instrument shown in the bottom panel.

ORCID iDs

Michael J. Koss https://orcid.org/0000-0002-7998-9581
Claudio Ricci https://orcid.org/0000-0001-5231-2645
Benny Trakhtenbrot https://orcid.org/0000-0002-3683-7297
Kyuseok Oh https://orcid.org/0000-0002-5037-951X
Jakob S. den Brok https://orcid.org/0000-0002-8760-6157
Julian E. Mejía-Restrepo https://orcid.org/0000-0001-8450-7463
Daniel Stern https://orcid.org/0000-0003-2686-9241
George C. Privon https://orcid.org/0000-0003-3474-1125
Ezequiel Treister https://orcid.org/0000-0001-7568-6412
Meredith C. Powell https://orcid.org/0000-0003-2284-8603
Richard Mushotzky https://orcid.org/0000-0002-7962-5446
Franz E. Bauer https://orcid.org/0000-0002-8686-8737
Tonima T. Ananna https://orcid.org/0000-0001-8211-3807
Mislav Baloković https://orcid.org/0000-0003-0476-6647
Rudolf E. Bär https://orcid.org/0000-0001-5481-8607
George Becker https://orcid.org/0000-0003-2344-263X
Patricia Bessiere https://orcid.org/0000-0002-0205-5940
Leonard Burtscher https://orcid.org/0000-0003-1014-043X
Turgay Caglar https://orcid.org/0000-0002-9144-2255
Enrico Congiu https://orcid.org/0000-0002-8549-4083
Phil Evans https://orcid.org/0000-0002-8465-3353
Marianne Heida https://orcid.org/0000-0002-1082-7496
Kohei Ichikawa https://orcid.org/0000-0002-4377-903X
Nikita Kamraj https://orcid.org/0000-0002-3233-2451
Isabella Lamperti https://orcid.org/0000-0003-3336-5498
Fabio Pacucci https://orcid.org/0000-0001-9879-7780
Federica Ricci https://orcid.org/0000-0001-5742-5980
Rogério Riffel https://orcid.org/0000-0002-1321-1320
Alejandra F. Rojas https://orcid.org/0000-0003-0006-8681
Kevin Schawinski https://orcid.org/0000-0001-5464-0888
Matthew J. Temple https://orcid.org/0000-0001-8433-550X

C. Megan Urry https://orcid.org/0000-0002-0745-9792
Sylvain Veilleux https://orcid.org/0000-0002-3158-6820
Jonathan Williams https://orcid.org/0000-0002-0441-3502

References

Ahumada, R., Allende Prieto, C., Almeida, A., et al. 2020, ApJS, 249, 3
Aliu, E., Archambault, S., Arlen, T., et al. 2012, ApJ, 759, 102
Ananna, T. T., Weigel, A. K., Trakhtenbrot, B., et al. 2022, ApJS, 261, 9
Anderson, S. F., Margon, B., Voges, W., et al. 2007, AJ, 133, 313
Angioni, R., Ros, E., Kadler, M., et al. 2019, A&A, 627, A148
Baek, J., Chung, A., Schawinski, K., et al. 2019, MNRAS, 488, 4317
Barthelmy, S. D., Barbier, L. M., Cummings, J. R., et al. 2005, SSRv, 120, 143
Bassani, L., Venturi, T., Molina, M., et al. 2016, MNRAS, 461, 3165
Baumgartner, W. H., Tueller, J., Markwardt, C. B., et al. 2013, ApJS, 207, 19
Becker, G. D., Pettini, M., Rafelski, M., et al. 2019, ApJ, 883, 163
Berghea, C. T., Nelson, G. J., Rusu, C. E., Keeton, C. R., & Dudik, R. P. 2017, ApJ, 844, 90
Berney, S., Koss, M., Trakhtenbrot, B., et al. 2015, MNRAS, 454, 3622
Bodaghee, A., Rahoui, F., Tomsick, J. A., & Rodriguez, J. 2012, ApJ, 751, 113
Brandt, W. N., & Hasinger, G. 2005, ARA&A, 43, 827
Burtscher, L., Davies, R. I., Shimizu, T. T., et al. 2021, A&A, 654, A132
Cappellari, M. 2017, MNRAS, 466, 798
Cappellari, M., & Emsellem, E. 2004, PASP, 116, 138
Cappelluti, N., Ajello, M., Burlon, D., et al. 2010, ApJL, 716, L209
Cardelli, J. A., Clayton, G. C., & Mathis, J. S. 1989, ApJ, 345, 245
Collaboration, A., Robitaille, T. P., Tollerud, E. J., et al. 2013, A&A, 558, A33
Collin-Souffrin, S., Alloin, D., & Andrillat, Y. 1973, A&A, 22, 343
Comparat, J., Merloni, A., Dwelly, T., et al. 2020, A&A, 636, A97
Corral-Santana, J. M., Casares, J., Muñoz-Darias, T., et al. 2016, A&A, 587, A61
Courtois, H. M., Tully, R. B., Hoffman, Y., et al. 2017, ApJL, 847, L6
Davies, R. I., Burtscher, L., Rosario, D., et al. 2015, ApJ, 806, 127
de Martino, D., Papitto, A., Belloni, T., et al. 2015, MNRAS, 454, 2190
den Brok, J. S., Koss, M. J., Traktenbrot, B., et al. 2022, ApJS, 261, 7
Dwelly, T., Salvato, M., Merloni, A., et al. 2017, MNRAS, 469, 1065
Eckart, M. E., Stern, D., Helfand, D. J., et al. 2006, ApJS, 165, 19
Ficarra, A., Grueff, G., & Tomassetti, G. 1985, A&AS, 59, 255
Fortin, F., Chaty, S., Coleiro, A., Tomsick, J. A., & Nitschelm, C. H. R. 2018, A&A, 618, A150
Freudling, W., Romaniello, M., Bramich, D. M., et al. 2013, A&A, 559, A96
Ginsburg, A., & Mirocha, J. 2011, PySpecKit: Python Spectroscopic Toolkit, Astrophysics Source Code Library, ascl:1109.001
Green, P. J., Silverman, J. D., Cameron, R. A., et al. 2004, ApJS, 150, 43
Greene, J. E., & Ho, L. C. 2005, ApJ, 630, 122
Grupe, D., Wills, B. J., Leighly, K. M., & Meusinger, H. 2004, AJ, 127, 156
Halpern, J. P., Thorstensen, J. R., Cho, P., et al. 2018, AJ, 155, 247
Ho, L. C., & Kim, M. 2009, ApJS, 184, 398
Hunter, J. D. 2007, CSE, 9, 90
Husser, T. O., Wende-von Berg, S., Dreizler, S., et al. 2013, A&A, 553, A6
Jones, D. H., Read, M. A., Saunders, W., et al. 2009, MNRAS, 399, 683
Jones, D. H., Saunders, W., Colless, M., et al. 2004, MNRAS, 355, 747
Karasev, D. I., Lutovinov, A. A., Revnivtsev, M. G., & Krivonos, R. A. 2012, AstL, 38, 629
Kausch, W., Noll, S., Smette, A., et al. 2015, A&A, 576, A78
Kennedy, M. R., Breton, R. P., Clark, C. J., et al. 2020, MNRAS, 494, 3912
Kormendy, J., & Ho, L. C. 2013, ARA&A, 51, 511
Kosec, P., Brightman, M., Stern, D., et al. 2017, ApJ, 850, 168
Koss, M., Mushotzky, R., Treister, E., et al. 2011, ApJL, 735, L42
Koss, M., Mushotzky, R., Treister, E., et al. 2012, ApJL, 746, L22
Koss, M., Mushotzky, R., Veilleux, S., & Winter, L. 2010, ApJL, 716, L125
Koss, M., Trakhtenbrot, B., Ricci, C., et al. 2017, ApJ, 850, 74
Koss, M. J., Assef, R., Baloković, M., et al. 2016a, ApJ, 825, 85
Koss, M. J., Blecha, L., Bernhard, P., et al. 2018, Nature, 563, 214
Koss, M. J., Glidden, A., Baloković, M., et al. 2016b, ApJL, 824, L4
Koss, M. J., Strittmatter, B., Lamperti, I., et al. 2021, ApJS, 252, 29
Koss, M. J., Trakhtenbrot, B., Ricci, C., et al. 2022a, ApJS, 261, 1
Koss, M. J., Trakhtenbrot, B., Ricci, C., et al. 2022b, ApJS, 261, 6
Lamperti, I., Koss, M., Trakhtenbrot, B., et al. 2017, MNRAS, 467, 540
Leroy, A. K., Sandstrom, K. M., Lang, D., et al. 2019, ApJS, 244, 24
Lidman, C., Courbin, F., Meylan, G., et al. 1999, ApJL, 514, L57
Liu, Q. Z., van Paradijs, J., & van den Heuvel, E. P. J. 2001, A&A, 368, 1021
Lusso, E., Comastri, A., Vignali, C., et al. 2011, A&A, 534, A110
Mahony, E. K., Croom, S. M., Boyle, B. J., et al. 2010, MNRAS, 401, 1151
Marconi, A., Risaliti, G., Gilli, R., et al. 2004, MNRAS, 351, 169
Marshall, J. L., Burles, S., Thompson, I. B., et al. 2008, Proc. SPIE, 7014, 701454
Massaro, E., Giommi, P., Leto, C., et al. 2009, A&A, 495, 691
McLure, R. J., & Dunlop, J. S. 2002, MNRAS, 331, 795
McQuinn, K. B. W., Skillman, E. D., Dolphin, A. E., Berg, D., & Kennicutt, R. 2017, AJ, 154, 51
Mejía-Restrepo, J., Koss, M. J., Trakhtenbrot, B., et al. 2022, ApJS, 261, 5
Mejia-Restrepo, J. E., Trakhtenbrot, B., Lira, P., Netzer, H., & Capellupo, D. M. 2016, MNRAS, 460, 187
Menzel, M. L., Merloni, A., Georgakakis, A., et al. 2016, MNRAS, 457, 110
National Optical Astronomy Observatories 1999, IRAF: Image Reduction and Analysis Facility, Astrophysics Source Code Library, ascl:9911.002
Oda, S., Ueda, Y., Tanimoto, A., & Ricci, C. 2018, ApJ, 855, 79
Oh, K., Koss, M., Markwardt, C. B., et al. 2018, ApJS, 235, 4
Oh, K., Schawinski, K., Koss, M., et al. 2017, MNRAS, 464, 1466
Oh, K., Koss, M. J., Ueda, Y., et al. 2022, ApJS, 261, 4
Oke, J. B., Cohen, J. G., Carr, M., et al. 1995, PASP, 107, 375
Paliya, V. S., Koss, M., Trakhtenbrot, B., et al. 2019, ApJ, 881, 154
Pfeifle, R. W., Ricci, C., Boorman, P. G., et al. 2022, ApJS, 261, 3
Predehl, P., Andritschke, R., Arefiev, V., et al. 2021, A&A, 647, A1
Puccetti, S., Comastri, A., Bauer, F. E., et al. 2016, A&A, 585, A157
Ricci, C., Ho, L. C., Fabian, A. C., et al. 2018, MNRAS, 480, 1819
Ricci, C., Trakhtenbrot, B., Koss, M. J., et al. 2017a, ApJS, 233, 17
Ricci, C., Trakhtenbrot, B., Koss, M. J., et al. 2017b, Nature, 549, 488
Ricci, F., Treister, E., Bauer, F. E., et al. 2022, ApJS, 261, 8
Rojas, A. F., Masetti, N., Minniti, D., et al. 2017, A&A, 602, A124
Rojas, A. F., Sani, E., Gavignaud, I., et al. 2020, MNRAS, 491, 5867
Schlegel, D. J., Finkbeiner, D. P., & Davis, M. 1998, ApJ, 500, 525
Shappee, B. J., Prieto, J. L., Grupe, D., et al. 2014, ApJ, 788, 48
Shen, Y., Richards, G. T., Strauss, M. A., et al. 2011, ApJS, 194, 45
Shimizu, T. T., Davies, R. I., Koss, M., et al. 2018, ApJ, 856, 154
Silverman, J. D., Mainieri, V., Salvato, M., et al. 2010, ApJS, 191, 124
Sluse, D., Sonnenfeld, A., Rumbaugh, N., et al. 2017, MNRAS, 470, 4838
Smette, A., Sana, H., Noll, S., et al. 2015, A&A, 576, A77
Smith, K. L., Koss, M., & Mushotzky, R. F. 2014, ApJ, 794, 112
Smith, K. L., Mushotzky, R. F., Koss, M., et al. 2020, MNRAS, 492, 4216
Stocke, J. T., Morris, S. L., Gioia, I. M., et al. 1991, ApJS, 76, 813
Szokoly, G. P., Bergeron, J., Hasinger, G., et al. 2004, ApJS, 155, 271
Tomsick, J. A., Chaty, S., Rodriguez, J., Walter, R., & Kaaret, P. 2008, ApJ, 685, 1143
Tomsick, J. A., Chaty, S., Rodriguez, J., Walter, R., & Kaaret, P. 2009, ApJ, 701, 811
Trakhtenbrot, B., & Netzer, H. 2012, MNRAS, 427, 3081
Treister, E., Virani, S., Gawiser, E., et al. 2009, ApJ, 693, 1713
Tremonti, C. A., Heckman, T. M., Kauffmann, G., et al. 2004, ApJ, 613, 898
Tully, R. B., Rizzi, L., Shaya, E. J., et al. 2009, AJ, 138, 323
Tzanetakis, A., Spencer, R. E., Masson, C. R., & Baldwin, J. E. 1978, MNRAS, 185, 63P
van der Walt, S., Colbert, S. C., & Varoquaux, G. 2011, CSE, 13, 22
Vasudevan, R. V., & Fabian, A. C. 2009, MNRAS, 392, 1124
Vazdekis, A., Ricciardelli, E., Cenarro, A. J., et al. 2012, MNRAS, 424, 157
Vernet, J., Dekker, H., D'Odorico, S., et al. 2011, A&A, 536, A105
Vestergaard, M., & Peterson, B. 2006, ApJ, 641, 689
Voges, W., Aschenbach, B., Boller, T., et al. 1999, A&A, 349, 389
Winn, J. N., Kochanek, C. S., McLeod, B. A., et al. 2002, ApJ, 575, 103
Yates, R. M., Kauffmann, G., & Guo, Q. 2012, MNRAS, 422, 215
York, D. G., Adelman, J., Anderson, J. E. J., et al. 2000, AJ, 120, 1579
Yukita, M., Ptak, A., Hornschemeier, A. E., et al. 2017, ApJ, 838, 47